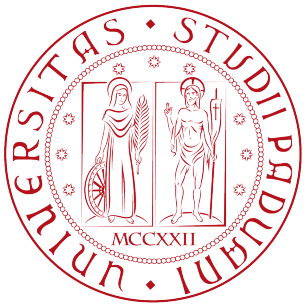

UNIVERSITÀ DEGLI STUDI DI PADOVA

Dipartimento di Fisica e Astronomia "Galileo Galilei"

Master Degree in Physics

Final Dissertation

Magneto-thermal evolution of neutron stars:

a 3D approach

Thesis supervisor

Prof. Roberto Turolla

Thesis co-supervisor

Dr. Davide De Grandis

Candidate

Andrea Gnarini

Academic Year 2019/2020

Abstract

Neutron stars (NSs) are the endpoints of the evolution of massive stars ($8M_\odot \lesssim M \lesssim 25M_\odot$), the remnants of the core collapse which follows the supernova explosion which marks the death of the progenitor. With a mass of the order of the solar mass and a radius of only 10-15 km, NSs are the most compact stellar objects in the present universe, reaching higher densities than those of atomic nuclei. Besides, they are endowed with extremely strong magnetic, the highest recorded to date.

NSs are born very hot ($T \approx 10^{11}$ K), and cool down as they age. Their thermal evolution is inherently coupled to that of their magnetic field. Knowledge of the secular magneto-thermal evolution can discriminate between different cooling scenarios when compared to observations, thus constraining the equation of state (EOS) of ultra-dense matter. Moreover, it provides a self-consistent map of the surface temperature, which is key in deriving any reliable estimate of the star radius from X-ray observations. This, again, directly bears to the determination of the NS EOS.

The aim of this study is to model the evolution of the temperature and the magnetic field in the NS crust by means of numerical simulations performed with PARODY, a 3D, pseudo-spectral code which solves the coupled induction and temperature equations in the crust of an highly-magnetised isolated NS ($B \gtrsim 10^{14}$ G). A fully 3D approach is required in order to treat non-axysimmetric magnetic configurations and the explore small-scale structures which naturally arise as a consequence of the Hall term, the role of which has been recently elucidated.

As in previous studies on the subject, we compute the magnetic field and temperature evolution in the NS crust, relying on the assumption that the Meissner effect is able to expel any magnetic flux from the type I, superconducting core on a timescale shorter than the typical timescales of magnetic and thermal evolution. We present in this work some of the first 3D magneto-thermal simulations, considering different initial configurations for the magnetic field. We start with axisymmmetric cases, to have a better comparison with previous investigations, and then turn to non-axisymmetric models, for which a 3D approach is indeed necessary for a complete study of the magnetic topology and the temperature configuration in the crust.

Sommario

Le stelle di neutroni (NS) sono lo stadio evolutivo finale di stelle con massa sufficientemente elevata, i resti del nucleo collassano a seguito dell'esplosione di una supernova che segna la morte del progenitore. Con una massa dell'ordine di quella solare e un raggio di solo 10-15 km, esse sono i corpi più compatti dell'universo, raggiungendo densità maggiori dei nuclei atomici. Inoltre, sono dotate di campi magnetici estremamente forti, i cui valori sono i più alti registrati ad oggi.

Le NS nascono con alte temperature ($T \approx 10^{11}$ K), e si raffreddano invecchiando. La loro evoluzione termica é intrinsecamente legata a quella del loro campo magnetico. Facendo un confronto con le osservazioni, la conoscenza dell'evoluzione secolare magneto-termica permette una distinzione tra diversi scenari di raffreddamento, vincolando, quindi, l'equazione di stato (EOS) della materia ultra-densa. Inoltre, fornisce una mappa auto-consistente della temperatura superficiale, che rappresenta la chiave per derivare una stima affidabile del raggio della stella a partire dalle osservazioni in banda X. Questo porta alla determinazione della EOS per le NS.

Lo scopo di questo studio è di creare un modello per l'evoluzione della temperatura e delle componenti del campo magnetico nella crosta delle NS attraverso simulazioni numeriche eseguite con PARODY, un codice 3D pseudo-spettrale che risolve l'equazione di induzione accoppiata con quella per la temperatura nella la crosta di una NS isolata con un campo magnetico molto intenso ($B \gtrsim 10^{14}$ G).

È necessario, dunque, un approccio interamente in 3D per trattare le configurazioni magnetiche non-asimmetriche ed esplorare le strutture su piccola scala che derivano direttamente dal termine di Hall, il cui ruolo é stato recentemente delucidato.

Come fatto in precedenti studi sull'argomento, calcoliamo il campo magnetico e l'evoluzione della temperatura della crosta della NS, basandoci sul presupposto che l'effetto Meissner é in grado di espellere qualunque flusso magnetico dal nucleo superconduttivo di tipo I, in un tempo minore rispetto a quelli dell'evoluzione magnetica e termica.

In questo lavoro presentiamo alcune delle prime simulazioni 3D magneto-termiche, considerando diverse configurazioni iniziali per il campo magnetico. Iniziamo dai casi assisimmetrici, per poter fare un miglior paragone con i precedenti studi, per poi considerare i modelli non-assisimmetrici, per cui é certamente necessario un approccio 3D per fare uno studio completo della topologia magnetica e della configurazione della temperatura nella crosta e sulla superficie.

Contents

Introduzione **1**

1 Neutron Stars **3**
1.1 Structure . . . 3
1.2 Outer Crust . . . 5
1.3 Inner Crust . . . 7
1.4 Superfluidity and Superconductivity . . . 9
1.5 Global Structure . . . 10

2 Neutron Star Cooling **13**
2.1 Neutrino Emission . . . 14
2.2 Photon Emission . . . 16
2.3 Neutrino Emission in the Crust . . . 18
2.4 Thermal Conductivity . . . 20

3 Magneto-Thermal Evolution **23**
3.1 Magneto-Hydrodynamics . . . 23
3.2 Hall Induction Equation in eMHD . . . 24
3.3 Evolution Equations in a NS Crust . . . 25
3.4 Poloidal-Toroidal decomposition . . . 28

4 Numerical Implementation **29**
4.1 Spectral Decomposition . . . 29
4.2 Spectral Algorithms . . . 30
4.3 Boundary Conditions . . . 30
4.4 Initial Conditions . . . 31

5 Numerical 3D Simulations **33**
5.1 Axisymmetric Configurations . . . 33
5.1.1 Dipole Configuration . . . 33
5.1.2 Hall Attractor . . . 35
5.2 Non-Axisymmetric Configuration . . . 37

6 Conclusions and Future Perspectives **45**
6.1 Discussion . . . 45
6.2 Future Applications . . . 46

A Special Functions **49**
A.1 Legendre Polynomials . . . 49
A.2 Spherical Bessel Functions . . . 50
A.3 Jacobi Polynomials . . . 51

Introduction

Neutron stars are one of the possible endpoint of stellar evolution and the most compact objects with a surface in the universe. With masses of $1 - 2\,M_\odot$ (where $M_\odot = 1.99 \cdot 10^{33}\,\mathrm{g}$ is the solar mass) and radii of about $10 - 15\,\mathrm{km}$ (10^5 smaller than the solar radius), their central density reaches $\sim 10^{15}\,\mathrm{g\,cm^{-3}}$ comparable and even larger than nuclear saturation density. Furthermore, NSs spin very fast with typical periods of the order of $P \sim (10^{-3} - 10)\,\mathrm{s}$.

The existence of astrophysical objects supported by the neutron degenerate gas pressure, in analogy to the case of white dwarfs which are supported by electron degenerate gas pressure, was first proposed in the 1930s by Baade and Zwicky (1934) and even before by Landau (1932) and then confirmed later on with the discovery of Pulsars. Landau improvised the concept of neutron stars in a discussion with N. Bohr and L. Rosenfeld in March 1931, before the discovery of the neutron by J. Chadwick. In 1937, G. Gamow and Landau independently suggested that any star could contain a NS in its core. This would have initiated a slow "accretion" of stellar matter onto its core, so that the stellar energy could have been supplied by the gravitational energy release during the accretion. However, very soon the idea was almost forgotten since Bethe and Critchfield (1938) showed that the energy of stars is provided by thermonuclear reactions.

The next most important step was done by Tolman (1939) and independently by Oppenheimer and Volkoff (1939) who derived the equation of hydrostatic equilibrium for a spherically symmetric star in the framework of General Relativity. The Tolman-Oppenheimer-Volkoff (TOV) equation is the basic relation for building a NS model, once an equation of state (EOS) is fixed.

Until the beginning of the 1960s, NSs had been treated as the work of theoreticians and the theory had been developing slowly. The first simplified calculations of the NS cooling were proposed in mid '60s, emphasizing the strong dependence of the cooling rate on neutrino emission processes and pointing out that this dependence can be used to explore the EOS of dense matter by comparing theoretical cooling models with observations of thermal radiation from NSs. The situation started changing later, with the hope to discover NS in observations. In particular, the first object to be identified as a NS was the pulsating star at the center of the Crab Nebula in 1967 (Hewish et al., 1968).

Neutron stars harbour extremely strong magnetic fields within their solid outer crust which are the strongest presently known in the universe, with typical values $B \sim 10^{10} - 10^{13}\,\mathrm{G}$ and up to $10^{15}\,\mathrm{G}$ in ultra-magnetized neutron stars, the so-called *magnetars* (Duncan and Thompson, 1992). This broad range of magnetic field intensities combined with the fact that magnetars show activity powered by the magnetic field and usually have relatively young inferred ages provides evidence that the magnetic field evolves with time. Moreover, NSs cool down as they age and their thermal evolution is coupled to that of their magnetic field, described by the Hall induction equation. The magneto-thermal evolution can be model with

the help of a fully 3D pseudo-spectral code (PARODY) for numerical simulations. The aim of this work, one of the first using a fully 3D approach, is to illustrate the basic equations governing the magneto-thermal evolution of an isolated highly-magnetised NS and present the results of some simulations exploring different kind of initial conditions, with the focus on non-axisymmetric configurations. The work is organized as follows:

- in Chapter 1, the general structure of NSs are reviewed, including general relativistic structure equations and, in particular, focusing the attention on the crust structure and its properties;
- in Chapter 2, the main cooling processes occuring in a NS core are decribed through the thermal evolution equation together with the role of neutrinos;
- in Chapter 3, starting from the electron magneto-hydrodynamics (eMHD), we derived Hall induction equation describing the magnetic field evolution in the crust. Then, this can be coupled with the thermal evolution equation;
- in Chapter 4, the main characteristics of the code are described together with the boundary and initial conditions for our simulations;
- in Chapter 5, the results of a number of magneto-thermal simulations of a NS provided by PARODY are illustrated for a range of different initial configurations of the magnetic field, considering both axisymmetric and non-axisymmetric topologies.

1. Neutron Stars

Neutron stars are from the a gravitational core-collapse Supernova of a star with quite high mass, $8M_\odot \lesssim M \lesssim 25M_\odot$. Massive stars ($M \gtrsim 8\,M_\odot$), at variance with solar mass stars, can proceed past the He-burning phase and arrive to synthesize elements of the iron group. When the core is mainly made of Fe and Ni, no other exothermic nuclear fusion reactions can take place and the high temperature causes the photo-disintegration of nuclei and neutrino production and emission. With no pressure support, the core collapses under its own gravity, the density starts to increase and at $\rho \gtrsim 10^{14}\,\mathrm{g\,cm^{-3}}$, nuclei are completely broken up and matter is mainly composed by neutrons. If the star has sufficiently high mass, the degeneracy pressure of neutrons can stop the collapse and trigger a shock that propagating outward blows up the star envelope (*Supernova event*).

1.1 Structure

A neutron star can be divided in different layered regions as shown in Figure 1.1 (Haensel et al., 2007):

- The outer region (*Atmosphere*) is a thin plasma layer composed of heavy elements (Fe, Ni) and possibly H and He coming from accreted interstellar medium. The atmosphere layer is very thin due to the strong gravity of the neutron star, but can be optically thick.
- The *envelope* (or *ocean*) is about 100 m thick and is made up of a Coulomb liquid of ions and electrons with relatively low density ($\rho \lesssim 10^9\,\mathrm{g\,cm^{-3}}$). It is the region with largest temperature and pressure gradients while density decreases down smoothly. Together with the atmosphere represents only a very small fraction of the total mass.
- The outer part of the *crust* is mainly composed by a Coulomb lattice of ^{56}Fe nuclei, free neutrons and ultra-relativistic degenerate electrons. The nuclei are more and more neutron rich as the density grows ($\rho \geq 10^7\,\mathrm{g\,cm^{-3}}$) as the result of electron capture. The transition between the crust and the envelope takes place at density below which the matter is in a liquid state. Free degenerate neutrons, electrons and heavy nuclei make up the *inner crust*. The thickness of the entire crust is about 1 km.
- The next layer is the *mantle* in which the nuclei are condensed in a superfluid. Due to the high energy given by Coulomb interaction, nuclei are deformed into cylindrical or planar forms (*nuclear pasta*). The existence of the mantle is strictly correlated to the stability of nuclei and its very existence is hence debeated.
- The *outer core* that has extremely high densities ($0.5\rho_0 \lesssim \rho \lesssim 2\rho_0$, where

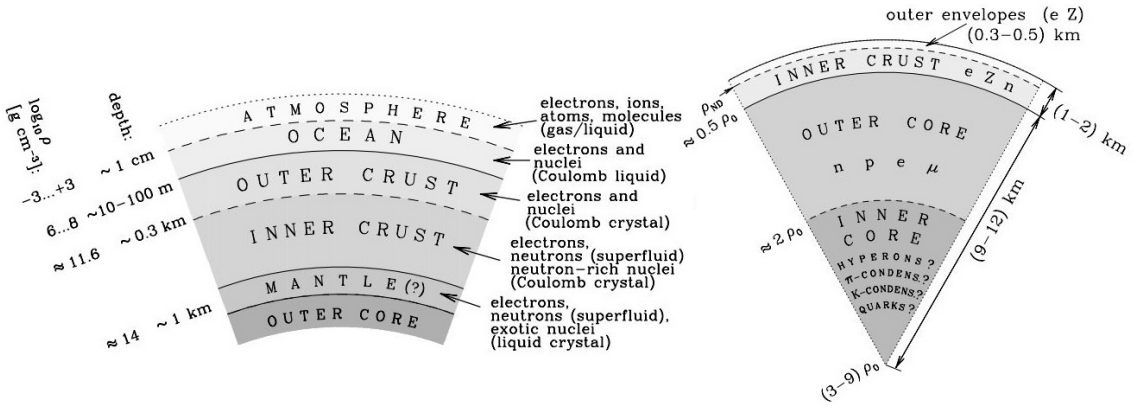

Figure 1.1: Schematic representation of a neutron star structure (Haensel et al., 2007).

ρ_0 is the normal nuclear density) at which matter consists in a plasma of protons, neutrons and leptons (*npeμ-matter*). The thickness of the outer core is generally of the order of few kilometers and it makes up the bulk of the NS mass.

- The central part (*inner core*) has very high density and it exists only for stars with $M \gtrsim 1.5\,M_\odot$. The inner core composition is still not well understood. Classically, it is described as a superfluid of baryons most of which are neutrons. Neutrons degeneracy pressure can maintain the star against gravity. The presence of heavy particles, mainly Λ^- and Σ^+ hyperons, is also possible (*npeμΛΣ-matter*). But there is the possibility to have exotic state matter instead hyperons, like the formation of Bose-Einstein condensate of K or π mesons or a quark-gluon plasma.

For a cold non-accreting neutron star, complete thermodynamic equilibrium can be assumed with respect to all interactions at zero temperature. In this way, the matter will be in its ground state sketched in Figure 1.2. For a given baryon density n_B, charge neutrality and β-equilibrium, the ground state is the one that minimize the total energy density.

The β-equilibrium corresponds to the chemical equilibrium reached between *direct* and *inverse β-decay*:

$$\begin{cases} n \to e^- + p + \bar{\nu}_e \\ e^- + p \to n + \nu_e. \end{cases}$$

We know that only degenerate neutrons can provide the pressure to sustain the star against gravity. However, inverse β-decay may occur only if protons and electrons are completely degenerate because in this case their energy, which correspond to the Fermi energy, can make up for the proton-neutron mass defect $Q = m_n - m_p \simeq 2.5 m_e \simeq 1.3\,\mathrm{MeV}$. Complete degeneracy is reached in the limit of temperature going to zero and the Fermi-Dirac distribution function at thermodynamic equilibrium becomes

$$f(T) = \frac{1}{1 + \mathrm{e}^{(E-\mu)/T}} \xrightarrow{T\to 0} \Theta(E_F - E)$$

where μ is the chemical potential and $\Theta(E_F - E)$ is the Heaviside step function. We also define the *Fermi energy* as $E_F = \lim_{T\to 0} \mu(T)$. It means that for $E \leq E_F$ all quantum energy states are occupied. We can rewrite the Fermi energy also as:

$$E_F = mc^2 \sqrt{1 + x_F^2} \tag{1.1}$$

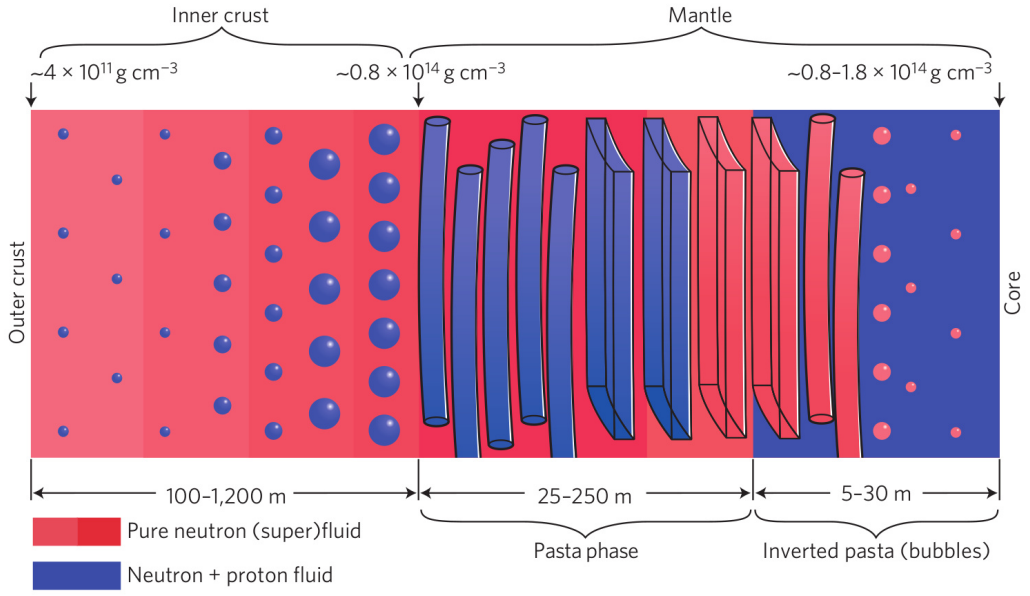

Figure 1.2: Schematic representation of the ground state structure of neutron stars as function of density or depth (Newton et al., 2011).

where x_F is the *adimensional Fermi momentum* defined as a function of the number density n:

$$x_F \equiv \frac{p_F}{mc} = \frac{h}{mc}\left(\frac{3n}{8\pi}\right)^{\frac{1}{3}}. \tag{1.2}$$

where $c = 2.99 \times 10^8\ \mathrm{m\,s^{-1}}$ is the speed of light and $h = 4.135 \times 10^{-15}\ \mathrm{eV\,s}$ is the Planck constant. In neutron stars we can always assume complete degeneracy for all the species because temperature is much lower than the Fermi temperature defined as $T_F = k_B E_F \simeq 10^{12}\,\mathrm{K}$. Furthermore, the density inside the neutron stars is so high that degenerate electrons also become relativistic ($x_{F,e} \gg 1$) while neutrons and protons remain non-relativistic ($x_{F,n}, x_{F,p} \ll 1$). Finally, the β-equilibrium can be expressed using the Saha equation for the chemical potentials equilibrium, neglecting the contribution of neutrino ($\mu_\nu = \mu_{\bar{\nu}} = 0$):

$$\mu_e + \mu_p = \mu_n. \tag{1.3}$$

Our main goal is to model the magneto-thermal evolution of a neutron star crust using also numerical simulations provided by PARODY (Chapter 4). So now we focus our attention more in detail on the crust structure.

1.2 Outer Crust

The total energy density for a given neutron star layer can be expressed as a sum of the energy of each nucleus $E(A, Z)$ with Z protons and $A - Z$ neutrons, the electron kinetic energy density ε_e and the lattice energy density ε_L taking account for all possible Coulomb (self)-interactions between electrons and ions:

$$\varepsilon_{\mathrm{tot}} = n_N E(A, Z) + \varepsilon_e + \varepsilon_L \tag{1.4}$$

being n_N the number density of nuclei.

Electrons can be assumed as a quasi-ideal Fermi gas for densities $\rho \gg 10AZ\,\mathrm{g\,cm^{-3}}$, so that their energy density is (Baym et al., 1971)

$$\varepsilon_e = \frac{m_e^4 c^2}{8\pi^2\hbar^3}\left[x_e(2x_e^2+1)\sqrt{x_e^2+1} - \ln(x_e+\sqrt{x_e^2+1})\right] \tag{1.5}$$

where x_e is the adimensional Fermi momentum for electrons. The effects of electron charge-screening can be neglected for dense and cold neutron star crusts.

To compute the lattice energy density, the crystal lattice of the crust is divided into many spheres centered (Wigner-Seitz cell approximation) around each nucleus with radius defined as

$$R_{cell} = \left(\frac{4\pi n_N}{3}\right)^{-1/3}. \tag{1.6}$$

The radius of these spheres is chosen so that their volume is exactly $1/n_N$ and each sphere contains the same number Z of electrons and protons, i.e. it is neutral. The lattice energy density is given by (Shapiro and Teukolsky, 1983)

$$\varepsilon_L = -\frac{9}{10}\left(\frac{4\pi}{3}\right)^{1/3} Z^{2/3} e^2 n_e^{4/3} \tag{1.7}$$

and does not take into account the nucleus Coulomb energy already inside $E(A,Z)$. We note that the total Coulomb energy is reduced by the lattice contribution ($\varepsilon_L < 0$).

From the total energy density (1.4), total pressure P can be derived as

$$P \equiv n_B^2 \frac{d}{dn_B}\left(\frac{\varepsilon_{\mathrm{tot}}}{n_B}\right) = P_e + \frac{1}{3}\varepsilon_L \tag{1.8}$$

where the dominant contribution comes from electrons, whose pressure P_e is defined as

$$P_e = \varepsilon_e - \mu_e n_e. \tag{1.9}$$

To determine the ground state structure of the crust, the total energy density $\varepsilon_{\mathrm{tot}}$ has to be minimized imposing charge neutrality. Since the baryon number density may show jumps or discontinuities due to the one-component plasma model assumption, the ground state can be found at $T = 0$ and at fixed pressure P (Chamel and Haensel, 2008). The pressure should be indeed continuous and monotonically increasing with respect to the depth. Hence the problem corresponds to minimizing the Gibbs free energy per nucleon at fixed pressure,

$$g(P) \equiv \frac{\varepsilon_{\mathrm{tot}} + P}{n_B} \tag{1.10}$$

and imposing charge neutrality, i.e. $n_p = n_e$.

The minimum energy configuration at $P = 0$ is reached for a body-centered-cubic (bcc) crystal lattice of ^{56}Fe with Gibbs free energy $g = E(^{56}\mathrm{Fe}) = 930.4\,\mathrm{MeV}$. This configuration remains the ground state of cold matter up to densities $\sim 10^6\,\mathrm{g\,cm^{-3}}$ at which matter composed by a plasma of nuclei and electrons is a nearly Fermi gas.

For higher densities, there is a jump of density every time that the ground state shifts to a different nucleus with smaller proton fraction, i.e. $(A,Z) \to (A',Z')$ (Haensel et al., 2007). The shift between the to two states is energetically advantageous and it is the reason why neutronization happens inside the nuclei.

Experimental nuclear data

$\rho_{\max}[\mathrm{g\,cm^{-3}}]$	Element	Z	N	R_{cell}[fm]
8.02×10^6	^{56}Fe	26	30	1404.05
2.71×10^8	^{62}Ni	28	34	449.48
1.33×10^9	^{64}Ni	28	36	266.97
1.50×10^9	^{66}Ni	28	38	259.26
3.09×10^9	^{86}Kr	36	50	222.66
1.06×10^{10}	^{84}Se	34	50	146.56
2.79×10^{10}	^{82}Ge	32	50	105.23
6.07×10^{10}	^{80}Zn	30	50	80.58

Skyrme model BSk8

$\rho_{\max}[\mathrm{g\,cm^{-3}}]$	Element	Z	N	R_{cell}[fm]
8.46×10^{10}	^{82}Zn	30	52	72.77
9.67×10^{10}	^{128}Pd	46	82	80.77
1.47×10^{11}	^{126}Ru	44	82	69.81
2.11×10^{11}	^{124}Mo	42	82	61.71
2.89×10^{11}	^{122}Zr	40	82	55.22
3.97×10^{11}	^{120}Sr	38	82	49.37
4.27×10^{11}	^{118}Kr	36	82	47.92

Table 1.1: Ground state structure of the outer crust of a neutron star computed using nuclear experimental data for $\rho \lesssim 6 \times 10^{10}\,\mathrm{g\,cm^{-3}}$ and the Skyrme model BSk8 for higher density (Rüster et al., 2006).

This reflects into a jump also of the baryon number density which arises from the pressure continuity

$$\frac{\Delta n_B}{n_B} \approx \frac{\Delta \rho}{\rho} \approx \frac{Z}{A}\frac{A'}{Z'} - 1.$$

For densities $\rho \lesssim 6 \times 10^{10}\,\mathrm{g\,cm^{-3}}$, the structure of the neutron star outer crust is completely determined by the data from nuclear experiments. At higher densities the matter composition is model dependent because the nucleus energy $E(A, Z)$ has to be computed and there are no experimental studies. The ground state structure of the outer crust is shown in Table 1.1 using experimental nuclear data and a Skyrme effective potential model BSk8 (Rüster et al., 2006).

1.3 Inner Crust

Going deeper towards the neutron star centre, as density increases the neutrons start to be less and less bound into nuclei and start to drip out forming a fermionic gas. The neutron drip point can be defined imposing a condition on the net neutron chemical potential for a neutron inside a nucleus

$$\mu_n' \equiv \mu_n - m_n c^2 = \left(\frac{\partial E(A,Z)}{\partial N}\right)_Z - m_n c^2. \tag{1.11}$$

Neutron drip happens when $\mu_n' = 0$, while if $\mu_n' < 0$, neutrons are all bound within nuclei. Performing the full calculation (Baym et al., 1971), the neutron drip density is $\rho_{ND} \approx 4 \times 10^{11}\,\mathrm{g\,cm^{-3}}$. The conformation of neutron star crust for densities beyond neutron drip relies on theoretical models only. Most of models are based on a purely classical analysis while others are semi-classical models, such as the Thomas-Fermi approximations and its extension (Negele and Vautherin, 1973).

An example of purely classical model is the *compressible liquid drop model*. The contribution to the energy density of the neutron gas must be included in the equation (1.4) as

$$\varepsilon_{\mathrm{tot}} = n_N E(A, Z) + \varepsilon_e + \varepsilon_L + \varepsilon_n \tag{1.12}$$

and the nuclei are treated as liquid drops of nuclear matter whose energy can be decomposed into volume, surface and Coulomb terms

$$E(A, Z) = E_{N,\mathrm{Vol}} + E_{N,\mathrm{Surf}} + E_{N,\mathrm{Coul}}$$

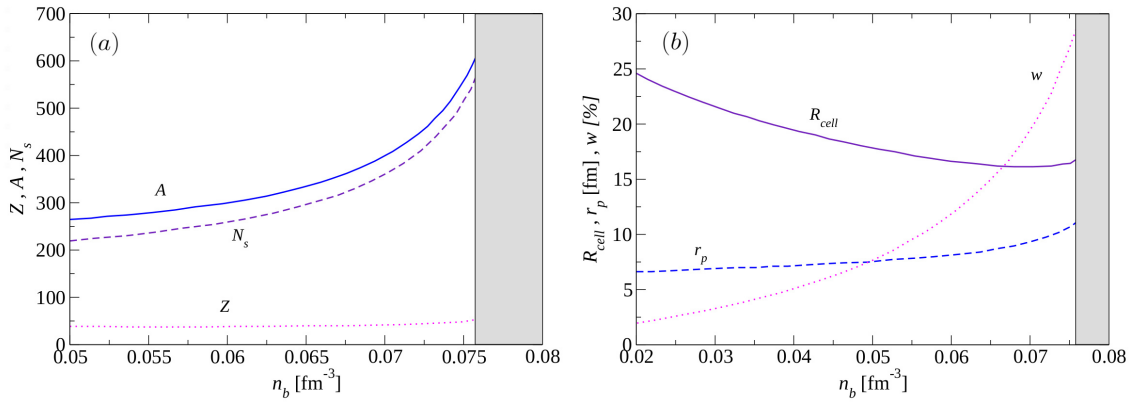

Figure 1.3: Composition of nuclear clusters (a) and structure (b) of the ground state of the inner crust as function of baryon number density n_B (Douchin and Haensel, 2000).

in which each terms can be parameterized in terms of A and Z.

It is easy to understand that the volume and surface energy terms are related respectively to the volume $\mathcal{V}_N$ and the surface area $\mathcal{A}_N$ of neutron clusters. The Coulomb energy for a uniformly-charge spherical drop of radius r_p can be computed as

$$E_{N,\mathrm{Coul}} = \frac{3}{5}\frac{Z^2e^2}{r_p}. \tag{1.13}$$

The electron contributions ε_e to the total energy density $\varepsilon_{\mathrm{tot}}$ is given by (1.5), while the lattice energy ε_L can be derived as

$$\varepsilon_L = -\frac{9}{10}\left(\frac{4\pi}{3}\right)^{1/3} Z^{2/3}e^2 n_e^{4/3}\left(1 - \frac{1}{3}\frac{r_p^2}{R_{\mathrm{cell}}^2}\right) \tag{1.14}$$

which is exactly the same form as before (1.7) with an additional correction related to the dimensions of the spherical drops compared to the cell ones.

As for the outer crust, the minimization of the total energy density $\varepsilon_{\mathrm{tot}}$ with respect to the free parameters of the model, imposing charge neutrality and fixing the baryon density n_B determines the structure of the nuclear matter.

Performing the full calculations (Haensel et al., 2007) neglecting the curvature corrections to the surface energy, the mechanical equilibrium condition for the crystal lattice reads

$$E_{N,\mathrm{surf}} = 2E_{N,\mathrm{Coul}} + 2\mathcal{V}_{\mathrm{cell}}\varepsilon_L. \tag{1.15}$$

The lattice energy density is very relevant for the equilibrium shape of the neutron cluster and can reduce the Coulomb energy term up to 15% at the neutron drip point. Moreover the equilibrium configuration is a result of the competition between Coulomb effects and surface effects, which favor respectively small and large clusters. We can also notice from the first plot of Figure 1.3 that the number of protons is almost constant in the inner crust, $Z \sim 40$, while the baryon number A and the number of neutrons on the surface of the cluster N_s are both increasing. As density increases, the distance between clusters decreases while their size r_p is almost constant and grows up a little at highest density (Figure 1.3 b).

This analysis of neutron stars inner crust structure is purely classical and do not take into account any quantum effects, which must be included in the treatment.

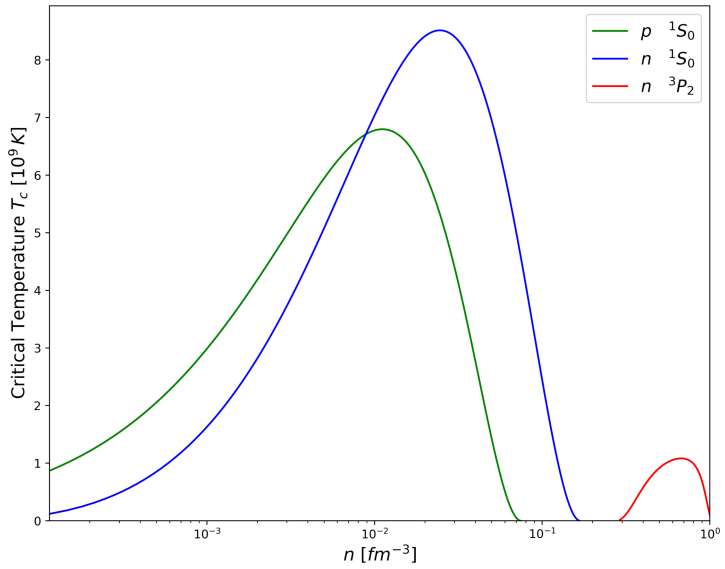

Figure 1.4: Critical temperatures for the onset of superfluidity as function of number density and for a given pairing type.

1.4 Superfluidity and Superconductivity

Inside a neutron star, nucleons can pair due to their attractive interactions (Bardeen et al., 1957). The BCS theory of electron superconductivity was successfully extended to nuclei by Bohr et al. (1958). In particular the strong interactions between neutrons, protons and possibly hyperons can provide attractive channels for pairing (Migdal, 1960).

The strength of the interaction determines the critical temperature $T_{\rm crit}$ at which the pairing phase transition occurs. Superfluidity disappears whenever the temperature exceeds the critical threshold. Performing full BCS theory calculation, it can be shown that the critical temperature is given by

$$T_{\rm crit} = \frac{\Delta_0}{k_B \gamma_g} \tag{1.16}$$

where γ_g is parameter depending on the pairing type and Δ_0 is the energy gap at zero temperature. A phenomenological formula for Δ_0 is given by (Kaminker, A. D. et al., 2001)

$$\Delta_0 = D \frac{(k_F - k_0)^2}{(k_F - k_0)^2 + k_1} \frac{(k_F - k_2)^2}{(k_F - k_2)^2 + k_3}$$

with $k_F = (3\pi^2 n)^{1/3}$ being the Fermi wavenumber and D, k_i related to the pairing type. The energy gap is vanishing outside the range $k_0 < k_F < k_2$.

The temperature dependence of the pairing gap, for $T \leq T_{\rm crit}$, can be approximately written as (Levenfish and Yakovlev, 1994)

$$\Delta_F(T) \simeq k_B T \sqrt{1 - \frac{T}{T_{\rm crit}}} \left(\alpha_g - \beta_g \sqrt{\frac{T_{\rm crit}}{T}} + \gamma_g \frac{T_{\rm crit}}{T} \right)$$

with α_g, β_g parameters related to the pairing type. Nucleons can pair in states with different angular momentum, this determines the kind of pairing. In the crust,

neutrons are expected to pair in $^1S_0$ states while in the core $^3P_2$. Also protons are expected to pair in $^1S_0$ states in the core of a neutron star. The net result is the a superfluid state related to neutron pairing, while the proton pairing also provides superconductivity.

The number density dependence of the critical temperature is reproduced in Figure 1.4 using values for D, k_i and γ_g taken from Ho et al. (2012). The maximum critical temperature for crustal neutrons is $T^{\max}_{\mathrm{crit},n} \simeq 8.5 \times 10^9$ K, while for protons in the core is a little lower, $T^{\max}_{\mathrm{crit},p} \simeq 7 \times 10^9$ K. Therefore, the transition to the superfluid and superconducting phase for neutron in the crust stars soon after birth. Moreover, the proton pairing ceases to exist at high densities, $\rho \gtrsim 10^{15}$ g cm^{-3}.

1.5 Global Structure

Spherically symmetry can be assumed for matter distribution in neutron stars to high accuracy. Deformations could be induced by very fast rotation ($P \lesssim 1$ ms) or extremely strong fields, $B \gtrsim 10^{18}$ G (Haskell et al., 2006). Present values of P and B, as derived from observations, are however outside these ranges.

To introduce general relativistic effects in neutron star structure and cooling, a space-time metric has to be considered. The equilibrium configuration of the neutron star crust is the result of the competition between pressure, electromagnetic and elastic stresses and the gravitational pull. The global structure can be derived from Einstein's equations

$$R_{\mu\nu} - \frac{1}{2} R g_{\mu\nu} = 8\pi T_{\mu\nu} \tag{1.17}$$

where $R_{\mu\nu}$ is the Ricci curvature tensor coming from the contraction of the Riemann curvature tensor, $R = g^{\mu\nu} R_{\mu\nu}$ is the Ricci scalar and $g_{\mu\nu}$ is the spacetime metric. The stress-energy tensor $T_{\mu\nu}$ takes into account pressure, electromagnetic and elastic stresses. Using spherical coordinated (r, θ, φ), it is possible to write the the most general form of a spherically symmetric spacetime (Misner et al., 1973) as

$$ds^2 = -\mathrm{e}^{2\Phi(r)} dt^2 + \mathrm{e}^{2\lambda(r)} dr^2 + r^2 (d\theta^2 + sin^2\theta d\varphi^2) \ . \tag{1.18}$$

The presence of matter for $r < R_*$, where R_* is the stellar radius, modifies the metric (*interior Schwarzschild solution*). Describing the matter as a perfect fluid of energy density ρ, isotropic pressure P and 4-velocity u^μ, the function λ in the metric coefficient can be computed as

$$\lambda(r) = -\frac{1}{2} \ln \left[1 - \frac{2m(r)}{r^2} \right]$$

while the lapse function $\mathrm{e}^{2\Phi(r)}$ is determined by

$$\frac{d\Phi(r)}{dr} = \frac{m(r)}{r^2} \left(1 + \frac{4\pi r^3 P}{m(r)} \right) \left(1 - \frac{2m(r)}{r} \right)^{-1} \tag{1.19}$$

with the boundary condition at the stellar radius $\mathrm{e}^{2\Phi(R_*)} = 1 - 2M/R_*$ where $M \equiv m(R_*)$ is the total gravitational mass of the central object. We define the enclosed gravitational mass within a radius r as

$$m(r) = 4\pi \int_0^r \rho(\tilde{r}) \tilde{r}^2 d\tilde{r}$$

where ρ is the mass-energy density. In empty space surrounding a spherically symmetric distribution of matter, i.e. $P = \rho = 0$, the *exterior* Schwarzschild's solution is recovered. The total radius of the star is determined by the condition $P(R) = 0$. The hydrostatic equilibrium condition in this configuration is described by the Tolman-Oppenheimer-Volkoff (TOV) equation (Oppenheimer and Volkoff, 1939; Tolman, 1939) and the pressure profile $P(r)$ is

$$\frac{dP(r)}{dr} = -(\rho + P)\frac{d\Phi(r)}{dr} \ . \tag{1.20}$$

The TOV equation completely determines the structure of a spherically symmetric body of isotropic material in equilibrium. We can recover Newtonian limit simply setting the exponential terms $e^{\lambda} = e^{\Phi} = 1$.

For a fluid mixture taking account also for superfluidity, the stress-energy tensor is given by (Carter and Langlois, 1998)

$$T^{\mu}_{\ \nu}{}^{(\mathrm{mix})} = \sum_X n_X^{\mu}\pi_{\nu}^X + \Psi\delta^{\mu}_{\nu}$$

where the sum runs over all matter constituents, π_ν is the particle momentum and Ψ is a generalized pressure. The electromagnetic contribution can be included into a term related to the electromagnetic tensor $F_{\mu\nu}$

$$T^{\mu}_{\ \nu}{}^{(\mathrm{em})} = \frac{1}{4\pi}F^{\mu\rho}F_{\nu\rho} - \frac{1}{8\pi}F^2\delta^{\mu}_{\nu}$$

For a rotating object such as a NS, the spherical symmetry is not valid anymore. However, the deviations from the static solution are negligible for typical spin values of neutron stars, i.e. the adimensional angular momentum is negligible, $a = J/M \ll 1$, where J is the angular momentum.

2. Neutron Star Cooling

The internal energy of a NS, and hence its temperature, changes in time because of the emission of radiation and neutrinos (Tsuruta and Cameron, 1966). In principle, also the energy losses due to gravitation wave emission should be taken into account. However, for an isolated neutron star, this can be neglected since the rotational speed and the quadrupole moment are quite small.

The energy equation, including general relativistic effects, describes the temperature evolution at each point of the neutron stars interior (Pons and Viganò, 2019; Thorne, 1977)

$$c_V \frac{\partial (T \mathrm{e}^{\Phi})}{\partial t} + \boldsymbol{\nabla} \cdot (\mathrm{e}^{2\Phi} \mathbf{F}) = \mathrm{e}^{2\Phi} (H - Q) \tag{2.1}$$

where c_V is the specific heat, H is the heating rate and Q the energy loss rate per unit volume repectively, which, in general are both function of the temperature T. The heat flux density $\mathbf{F}$ is defined in terms of the thermal conductivity tensor $\boldsymbol{k}$ as

$$\mathbf{F} = -\mathrm{e}^{-\Phi} \boldsymbol{k} \cdot \boldsymbol{\nabla} (\mathrm{e}^{\Phi} T) \tag{2.2}$$

and the nabla operator ∇ includes curvature effects

$$\nabla \equiv \left(\mathrm{e}^{-\lambda} \frac{\partial}{\partial r}, \frac{1}{r} \frac{\partial}{\partial \theta}, \frac{1}{r \sin \theta} \frac{\partial}{\partial \varphi} \right). \tag{2.3}$$

For a spherically symmetric isolated neutron star, the heat transfer equation (2.1) can be rewritten as two partial differential equations (Page et al., 2004):

$$\begin{cases} c_V \mathrm{e}^{\Phi} \dfrac{\partial T}{\partial t} + \dfrac{1}{4\pi r^2 \mathrm{e}^{\lambda}} \dfrac{\partial (L \mathrm{e}^{2\phi})}{\partial r} = \mathrm{e}^{2\Phi} (H - Q) \\ \dfrac{\partial (T \mathrm{e}^{\Phi})}{\partial r} = -\dfrac{\mathrm{e}^{\lambda}}{4\pi r^2 k} \mathrm{e}^{\Phi} \end{cases} \tag{2.4}$$

where L is the luminosity of the star and accounts for both photon and neutrino losses. The first one is due to photon emission from the surface of the star and is given by the Stefan-Boltzmann law for purely thermal emission. The second one, instead, is given by the energy loss via neutrino emission L_ν and depends on the neutrino production processes in the star crust and, mainly, in the core.

Matter inside a NS is highly degenerate, so that the specific heat per unit volume $\tilde{c}_V$ is the sum of all the contributions from each particle species (Page, 2009)

$$\tilde{c}_V = \sum_i \tilde{c}_{V,i} = \sum_i \left(\frac{m_i^* p_{F,i}}{3\pi^2 \hbar^3} \right) \pi^2 k_B^2 T$$

where $p_{F,i}$ and m_i^* are respectively the Fermi momentum and the effective mass for each species i. The specific heat c_V appearing in equation (2.4) is the integral of

$\tilde{c}_V$ over the whole volume of the star. However, the presence of superfluidity and superconductivity in the neutron stars interior can strongly alter the value of the specific heat c_V.

At relatively low temperature in any degenerate system of fermions with attractive interactions between particles Cooper pairs can arise (Cooper, 1956). In particular the strong interactions between neutrons, protons and possibly hyperons can provide effective channels for pairing (Migdal, 1960). When the temperature T is of the order of a critical temperature $T_{\rm crit}$, many pairs are formed but also broken down since $k_B T \gg \Delta(T)$ where Δ is the energy gap, i.e. half of the binding energy of a Cooper pair. The net effect is a jump in the specific heat c_V

$$c_V^{pair} = \mathcal{R}(T/T_{\rm crit}) \times c_V \tag{2.5}$$

where $\mathcal{R}$ is a coefficient taking account for the previous effects (Levenfish and Yakovlev, 1994).

2.1 Neutrino Emission

As shown in section 1.1, neutrino are produced in the core of a neutron star via direct and inverse β-decay (also known as *direct Urca* process)

$$n \to p + e^- + \bar{\nu}_e \quad \text{and} \quad e^- + p \to n + \nu_e.$$

Only if the energy and momentum conservation are satisfied, the previous two reactions can occur. The energy conservation simply becomes the chemical potential equilibrium (1.3) because for degenerate matter the energy of each particle is just the Fermi energy $E_{F,i} = \mu_i$ and the chemical equilibrium is always satisfied.

Momentum conservation for direct Urca reactions demands

$$p_{F,n} < p_{F,p} + p_{F,e}.$$

Because of charge neutrality $n_p = n_e$, i.e. $p_{F,p} = p_{F,e}$ from the definition of Fermi momentum, hence last relation reads $p_{F,n} < 2p_{F,p}$ or in terms of number density $n_n < 8n_p$. Defining now the *proton fraction* $R_p \equiv n_p/n_B$ with n_B the baryon number density, the momentum conservation for direct Urca requires

$$R_p \geq \frac{1}{9} \simeq 11\%. \tag{2.6}$$

Hence, to have the direct Urca processes take place, the number of protons must be of the order of 11 % of all baryons. For neutron stars only made of neutrons, protons and electrons (*npe-model*) the x_p-condition (2.6) can not be satisfied and the direct Urca is kinematically forbidden.

This condition is almost never reached even using more realistic EOS models except for some cases in the inner core in the presence of exotic state of matter, such as deconfined quark or charged meson condensate (Page, 2009). The direct Urca is allowed by conservation laws with other baryon species such as Λ hyperons

$$\Lambda \to p + e^- + \bar{\nu}_e \quad \text{and} \quad p + e^- \to \Lambda + \nu_e$$

or in deconfined quark matter

$$d \to u + e^- + \bar{\nu}_e \quad \text{and} \quad u + e^- \to d + \nu_e.$$

Let us consider instead the modified Urca (*mUrca*) process which is a standard Urca with a bystander particle x, which can be either a neutron or a proton. The presence of the bystander ensures the total momentum conservation:

$$n + x \to p + e^- + x + \bar{\nu}_e \quad \text{and} \quad p + e^- + x \to n + x + \nu_e$$

The main difference between the two processes is that the direct Urca is much more efficient than the modified Urca, i.e. the energy loss rate is much higher. The neutrino energy loss rate as function of temperature can be written as (Friman and Maxwell, 1979; Lattimer et al., 1991)

$$\begin{cases} \epsilon_\nu^{\mathrm{mUrca}} \approx 6.22 \times 10^{21} \alpha_n \, \beta_n \left(\dfrac{n_e}{n_0}\right)^{1/3} \left(\dfrac{m_n^*}{m_n}\right)^3 \left(\dfrac{m_p^*}{m_p}\right) T_9^8 \ \mathrm{erg\,cm^{-3}\,s^{-1}} \\ \epsilon_\nu^{\mathrm{dUrca}} \approx 4 \times 10^{27} \left(\dfrac{n_e}{n_0}\right)^{1/3} \dfrac{m_n^* m_p^*}{m_n^2} \, \Theta_{npe} \, T_9^6 \ \mathrm{erg\,cm^{-3}\,s^{-1}} \end{cases}$$

where $T_9 = T/10^9\,\mathrm{K}$, m_i^* are the effective particle mass, $n_0 = 0.16\,\mathrm{fm}^{-3}$ and Θ_{npe} is the step function, that is $\Theta_{npe} = 1$ if the Fermi momenta of neutrons, protons and electrons satisty the momentum conservation and $\Theta_{npe} = 0$ otherwise. Furthermore, $\alpha_n = 1.13$ and $\beta_n = 0.68$ are two parameters proposed by Friman and Maxwell (1979).

This reflects in different evolution timescales ranging from few second for direct Urca processes (*fast cooling* scenario) to months for modified Urca (*slow cooling* scenario). The energy lost via neutrino emission in the two cases can be computed by simply integrating the energy rate ϵ_ν over the volume:

$$\begin{aligned} L_\nu^{\mathrm{slow}} &= \int_V \epsilon_\nu^{\mathrm{mUrca}} dV = N_{\mathrm{s}} T^8, \\ L_\nu^{\mathrm{fast}} &= \int_V \epsilon_\nu^{\mathrm{dUrca}} dV = N_{\mathrm{f}} T^6. \end{aligned} \tag{2.7}$$

where N_{s} and N_{f} are two coefficients of proportionality including all the other dependencies. Considering the *neutrino cooling era* during which the energy loss via neutrino is dominant with respect to photon emission ($L_\nu \gg L_\gamma$) and remembering that, for a mixture of degenerate particles $c_V = cT$, the energy balance equation reduces to

$$cT \frac{dT}{dt} \simeq -L_\nu = -N_c T^a$$

where $a = 8$ or 6 depending on the Urca process choice. This simplified version of energy balance equation is valid in a Newtonian formulation and for an isothermal core. Young stars, for example, does not fulfil this assumption and they evolves differently toward isothermality. However, all observed neutron stars are old enough to consider their core at uniform temperature.

Fixing the initial conditions, the previous equation can be solved to find a relation between T and time t:

$$T \simeq \left[\frac{c}{(a-2)N_{\mathrm{c}}}\right]^{\frac{1}{a-2}} t^{-\frac{1}{a-2}}. \tag{2.8}$$

The neutrino energy loss rate is strongly modified in the presence of superfluidity and superconductivity. The net effect is very similar to the specific heat one and the energy loss rate for a process X changes according to

$$\epsilon_{\nu,X}^{\mathrm{pair}} = \mathcal{R}_X(T/T_c) \times \epsilon_{\nu,X} \ .$$

This results in a faster cooling evolution compared to the case without considering pairing and superfluidity.

2.2 Photon Emission

If the emission of photon is purely thermal, the photon luminosity is

$$L_\gamma = 4\pi R^2 \sigma T_s^4 \tag{2.9}$$

where $\sigma \simeq 5.67 \cdot 10^{-5}\,\mathrm{erg\,cm^{-2}\,s^{-1}\,K^{-4}}$ is the Stefan-Boltzmann constant and T_s is the surface effective temperature, i.e. the temperature of the blackbody that would radiate the same flux as the star. An external observer at large distances will observe a different luminosity due to gravitational redshift

$$L_\infty = 4\pi R_\infty^2 \sigma T_\infty^4 \tag{2.10}$$

where the quantities measured far away from the star are given in terms of those at the star surface by $R_\infty = \mathrm{e}^{-\Phi} R$ and $T_\infty = \mathrm{e}^{\Phi} T_s$, both potentially observable.

Similarly to what has been done for neutrinos, during the *photon cooling era* the energy loss via neutrino emission is negligible compared to photon luminosity ($L_\gamma \gg L_\nu$) so that the energy equation becomes:

$$cT\frac{dT}{dt} = -L_\gamma = -4\pi R^2 \sigma T_s^4.$$

A relation between the temperature at the outer core T and the surface temperature T_s is needed. The effect of the neutron star envelope is not negligible and the approach is to consider it separately using a plane-parallel approximation.

If no energy losses or gains occur in the envelope, the gradient of the temperature evaluated at the top of the crust will be (Tsuruta and Cameron, 1966):

$$-(\boldsymbol{k} \cdot \boldsymbol{\nabla} T) \cdot \hat{\mathbf{r}} = \sigma T_s^4(T, \mathbf{B}) \tag{2.11}$$

where the surface temperature has been chosen to be

$$T_s(T, g, B, \Theta) = T_s^{(0)}(T, g)\, \mathcal{X}(T, B, \Theta)\ , \tag{2.12}$$

g is the gravitational acceleration on the surface and $\mathcal{X}(T, B, \Theta)$ represents a magnetic correction (Potekhin and Yakovlev, 2001).

For an envelope mainly made of iron and not considering magnetic effects, $T_s^{(0)}$ has been exactly calculated by Gudmundsson et al. (1983) but can be modelled more in general as a power-law dependence (Tsuruta, 1964):

$$T_s \propto T^{\frac{1}{2}+\alpha}\ . \tag{2.13}$$

The photon luminosity (2.9) can be rewritten as

$$L_\gamma = 4\pi R^2 \sigma T_s^4 = S T^{2+4\alpha}.$$

Using Tsuruta law in the thermal evolution equation and solving it, one obtains

$$T = \left(\frac{c}{4\alpha S}\right)^{\frac{1}{4\alpha}} t^{-\frac{1}{4\alpha}}. \tag{2.14}$$

The evolution is very sensitive to the nature of the envelope since $\alpha \ll 1$ and to changes in the specific heat due to pairing.

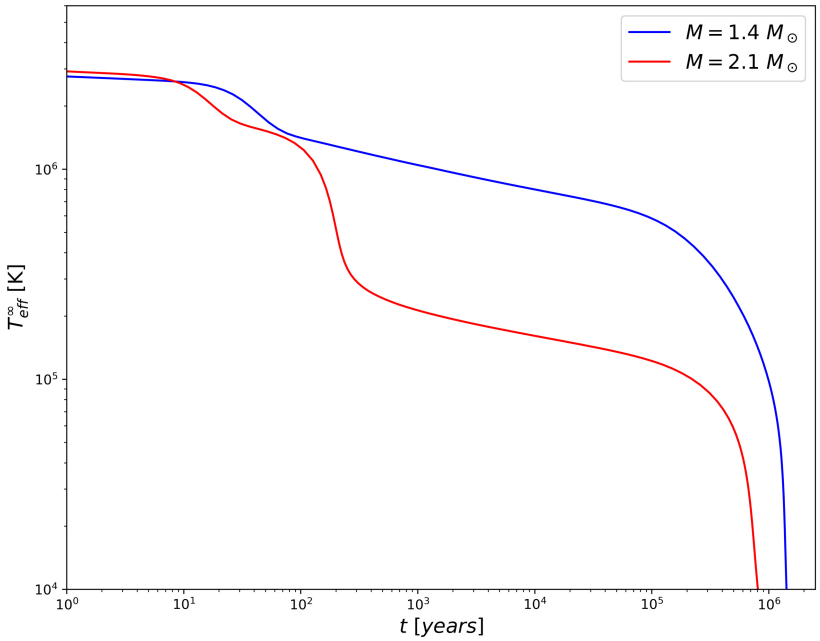

Figure 2.1: Examples of cooling curves for two standard neutron stars with $M = 1.4\ M_\odot$ and 2.1 $M_\odot$ corresponding to slow cooling (blue) and fast cooling (red) scenario.

The temperature T_* at which photon cooling starts to become important can be estimated by equating the photon luminosity L_γ to neutrino emission L_ν finding for slow/fast neutrino cooling scenario

$$T_*^{\rm s} \simeq \left(\frac{S}{N_{\rm s}}\right)^{\frac{1}{6}} \sim 10^8\,{\rm K} \quad \text{(Slow cooling scenario)}$$
$$T_*^{\rm f} \simeq \left(\frac{S}{N_{\rm f}}\right)^{\frac{1}{4}} \sim 10^6\,{\rm K} \quad \text{(Fast cooling scenario)}$$

In conclusion, three main cooling stages can be identified (Yakovlev et al., 2010):

i. The first stage (which can last for few centuries depending on the specific model) during which the core is thermally decoupled from the crust and the crustal neutrino emission dominates the cooling emission.
ii. The second neutrino cooling phase with isothermal core inside which neutrinos are produced ($10^2\,{\rm y} \lesssim t \lesssim 10^5\,{\rm y}$).
iii. The final stage, the photon cooling era, during which the main emission mechanism is the surface emission of thermal photons.

Up to now the effects due to magnetic field has been neglected, which is correct only for weakly magnetized NS ($B \lesssim 10^{12}$ G). Heating terms indeed can arise from the dissipation of magnetic field.

Examples of cooling curves are shown in Figure 2.1 for two standard neutron stars with $M = 1.4\ M_\odot$ and 2.1 $M_\odot$ which highlight the two different cooling scenarios: the blue curve, indeed, is an example of slow cooling scenario while for the red one direct Urca processes are active above a certain density. The cooling curves are derived with a 1D code develop by Page (2016).

2.3 Neutrino Emission in the Crust

Neutrino reactions in the neutron star crust are an important source of energy loss during the initial stages of the life of a star before the isothermal cooling phases (first $10-100$ years). These processes are associated with weak interaction between electrons, positrons, nuclei and free neutrons (Chamel and Haensel, 2008).

In our numerical simulations, the emission of neutrino entering in the heat equation (Section 3.3) is due to four dominant contributions

$$N_\nu(n,T,\mathbf{B}) = N_{\rm pair}(n,T) + N_{\rm ph}(n,T) + N_{\rm brem}(n,T) + N_{\rm syn}(n,T,\mathbf{B}) \tag{2.15}$$

where the phonon decay, the pair production, the neutrino bremsstrahlung and the neutrino synchroton emission are taken into account. Explicit relation for the four neutrino emissivities taken from Yakovlev et al. (2001), Ofengeim et al. (2014) and Kantor and Gusakov (2007) are implemented in our code.

In the presence of positrons, therefore at high temperature and low densities, a pair of neutrino can be produced by the annihilation of an electron-positrons pair (Chiu and Morrison, 1960)

$$e^- + e^+ \to \nu + \bar{\nu}.$$

In the case of non-degenerate electrons and positrons, i.e. $k_B T > \mu_e$, the neutrino emissivity for electron-positron pair annihilation can be estimated as

$$Q_\nu^{e\bar{e}-{\rm pair}} \propto n_{e^-} n_{e^+} \langle E_\nu \rangle \sigma_{e\bar{e}\to\nu\bar{\nu}} \propto T^9 \tag{2.16}$$

where $\langle E_\nu \rangle$ is the mean energy of neutrinos and $\sigma_{e\bar{e}\to\nu\bar{\nu}}$ is the cross section of the annihilation process (Yakovlev et al., 2001). With increasing density, in the limit of degenerate ultra-relativistic electrons $k_B T \ll \mu_e$, the positron density is exponentially smaller. Hence, the pair annihilation process is strongly suppressed for degenerate electrons.

Neutrino emission from the crust is dominated by *plasmon decay* and it is extremely efficient at high temperatures. A plasmon is a quantum of electromagnetic waves in a plasma and can be described classically ad an oscillation of electron density with respect to the fixed ions. A free electron cannot emit a neutrino pair since this is forbidden by energy-momentum conservation. However, if the electron is interacting with the surrounding medium, the energy is enough to trigger the plasmon $\bar{\gamma}$ decay process

$$\bar{\gamma} \to \nu + \bar{\nu}.$$

The total plasmon emissivity $\epsilon_{\rm pl}$ is the sum over the different flavors of neutrinos. Performing the full formal calculation (Yakovlev et al., 2001), the total emissivity can be computed using the dispersion relations for the plasma along the longitudinal and transversal directions in the limit of ultra-relativistic degenerate electrons at long wavelenght ($kc \ll \omega_{pe}$)

$$\omega_l^2 = \omega_{pe}^2 + \frac{3}{5}k^2c^2, \qquad \omega_t^2 = \omega_{pe}^2 + \frac{6}{5}k^2c^2 \tag{2.17}$$

where $\omega_{pe}^2 = 4\pi e^2 n_e / m_e^*$ is the electron plasma frequency and $k = 2\pi/\lambda$ the wavenumber. In the opposite regime, i.e. $kc \gg \omega_{pe}$, the longitudinal plasmons experience strong Landau damping and the transverse ones are transformed into ordinary electromagnetic waves.

The final expression for the plasmon neutrino emissivity is

$$Q_{\rm pl} \simeq \frac{G_F^2 c}{96\pi^4 e^2}\left(\frac{m_e c}{\hbar}\right)^9 I_{\rm pl} \tag{2.18}$$

where $G_F = 1.436 \times 10^{-49}\,{\rm erg\,cm^3}$ is the Fermi weak interaction constant and $I_{\rm pl} = I_l + I_t$ is the sum of two dimensionless functions, which in the high-temperature limit ($T \gg \omega_{pe}$) for ultra-relativistic degenerate electrons are (Braaten and Segel, 1993)

$$I_l = 0.349\frac{T\omega_{pe}^8}{m_e^9}, \qquad I_t = 16.227\frac{T^3\omega_{pe}^6}{m_e^9}$$

and the main contribution comes from the transverse plasmons. For low temperature the emissivity is exponentially suppressed due to the small number of plasmons. The emissivity grows as $Q_{\rm pl} \propto \rho^2$ since $\omega_{pe} \propto \rho^{1/3}$ in the high-temperature domain and it reaches the maximum value at $\omega_{pe} \sim T$.

For ground-state matter at neutron drip point ρ_{ND}, the electron plasma energy is very high, $\hbar\omega_{pe} \approx 1.5\,{\rm MeV}$. This means that the plasmon decay is effecient only at high temperatures in the early stages of neutron star cooling.

The plasmon decay is influenced by a strong magnetic field $\mathbf{B}$ because the plasma dispersion relation gets modified and, in particular, new plasma modes may appear. In general, the presence of $\mathbf{B}$ can alter the neutrino crustal emission and can make possible new channels of neutrino emission, such as electron synchrotron neutrino production (Kaminker et al., 1992). If we assume the magnetic field to be constant and uniform on microscopic scales, and directed along the z axis, it forces the electrons to rotate around the magnetic field lines. The electron momentum is not conserved, which opens the process

$$e \xrightarrow{B} e + \nu_l + \bar{\nu}_l$$

where B indicates that the process can occur only in the presence of magnetic field. The process is similar to the one happening with photons but much weaker. The calculation of the synchrotron emissivity $Q_{\rm syn}$ is analogous to the one for the pair annihilation process. Following a quasiclasiccal treatment (Kaminker et al., 1991) for typical temperature values, the synchrotron emissivity is independent of the electron number density and can be written as

$$Q_{\rm syn} \approx 9.04 \times 10^{14} B_{13}^2 T_9^5\ {\rm erg\,cm^{-3}\,s^{-1}} \tag{2.19}$$

where B_{13} is the magnetic field in units of 10^{13} G. Furthermore, $Q_{\rm syn}$ is indipendent of the electron mass and this implies that all plasma particles should, in principle, produce the same neutrino emission.

Some other processes might happen such as *photoneutrino emission*, but another major contribution comes from *neutrino Bremsstrahlung* from electron-neutron collisions (Kaminker et al., 1999)

$$e^- + (A, Z) \to e^- + (A, Z) + \nu + \bar{\nu}.$$

It proceeds via neutral and charged electro-weak currents and leads to the emission of neutrinos of all flavors. The general expression for the neutrino emissivity due to the neutrino-pair bremsstrahlung of the relativistic degenerate electrons in a plasma (Haensel et al., 1996) is

$$Q_{\rm br} \approx 3.23 \times 10^{17} \rho_{12} \frac{Z n_e}{n_B} T_9^6\, \mathcal{L}\ {\rm erg\,s^{-1}\,cm^{-3}} \tag{2.20}$$

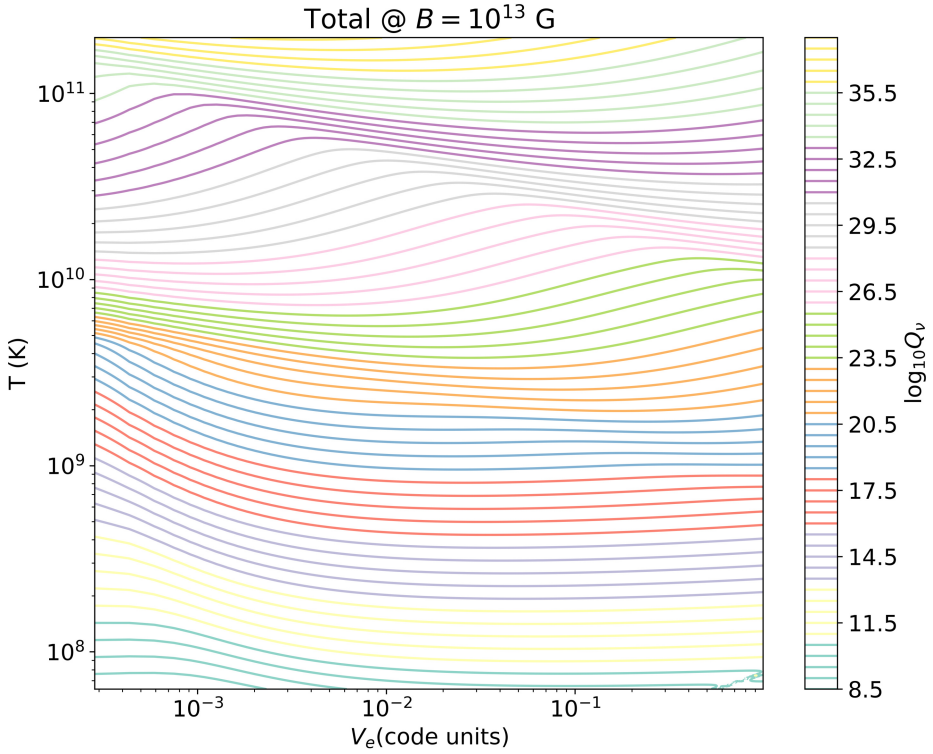

Figure 2.2: Total neutrino emissivity as function of temperature T and electron volume V_e at given magnetic field $B = 10^{13}$ G.

where ρ_{12} is the density in units of $10^{12}\,\mathrm{g\,cm^{-3}}$ and $\mathcal{L}$ is a dimensionless function made up of two terms coming from static-lattice contribution and from the electron scattering by the nuclear charge fluctuations due to lattice vibrations.

The total neutrino contribution can be represented as function of temperature T and electron volume V_e at given magnetic field $\mathbf{B}$ (Figure 2.2). The total emissivity (2.15) takes into account the plasmon decay, the electron-positron decay, weak bremsstrahlung and synchrotron emission.

2.4 Thermal Conductivity

Since in the previous analysis, the thermal conductivity κ has been treated as a scalar, we have assumed no anisotropies in the heat transport. However, in the presence of strong magnetic field, the heat flow may be anisotropic due the classical Larmor rotation, so that the thermal conductivity is no longer a scalar but becomes a tensor (Page, 2009). If the magnetic field $\mathbf{B}$ is along the z-axis, the conductivity can be written as

$$\boldsymbol{k} = \begin{pmatrix} \kappa_\perp & \kappa_\wedge & 0 \\ \kappa_\wedge & \kappa_\perp & 0 \\ 0 & 0 & \kappa_\parallel \end{pmatrix} \tag{2.21}$$

where the three components are

$$\kappa_\perp = \frac{\kappa_0}{1 + (\omega_B/\nu)^2}, \qquad \kappa_\wedge = \frac{\kappa_0}{1 + (\omega_B/\nu)^2}\frac{\omega_B}{\nu}, \qquad \kappa_\parallel = \kappa_0 \tag{2.22}$$

with $\omega_B = eB/m_e^* c$ being the electron gyrofrequency and ν is the collisional frequency. For strong anisotropy, i.e. $\omega_B \gg \nu$, the motion of electrons is controlled by the magnetic field so they move along the magnetic field lines and not perpendicularly to it, $\kappa_\perp \ll \kappa_\parallel, \kappa_0$. A strong magnetic field $\gtrsim 10^{10}$ G can also change the properties of heat transport.

According to the Wiedemann-Franz law, the thermal conductivity tensor $\boldsymbol{k}$ is related to the electron conductivity $\boldsymbol{\sigma}$ as

$$\boldsymbol{k} = \frac{\pi^2 k_B^2 T}{3e^2}\boldsymbol{\sigma}. \tag{2.23}$$

If the temperature of the crust is well below the electron degeneracy temperature but still above the ion plasma temperature, the electron conductivity can be divided into two terms

$$(\boldsymbol{\sigma}^{-1})_{ij} = \sigma^{-1}\delta_{ij} + \frac{\epsilon_{ijk}B_k}{ecn} \tag{2.24}$$

where the first term on the right-hand side is the symmetric part of the tensor

$$\sigma = e^2 c^2 \frac{n\tau_e(\mu)}{\mu} \tag{2.25}$$

with τ_e associated to the electron scattering as function of the electron chemical potential μ (Urpin and Yakovlev, 1980). The anti-symmetric part corresponds instead to the Hall drift effect (Pons and Geppert, 2007).

3. Magneto-Thermal Evolution

Having introduced the thermal evolution of a NS in the previous chapter, we now turn to the evolution of the star's magnetic field and on how this couples with the thermal one. We focus on the crustal magnetic field, since the core of NSs is in a superfluid and superconducting state (Type-I superconductor), so that the magnetic field is likely expelled via the Meissner effect from the core (Pons and Viganò, 2019). Indeed, in a region permeated by a magnetic field below a critical value, the superconductor exhibits a perfect diamagnetism expelling the field lines from the inside. This happens through the generation on the superconductor surface of currents inducing a magnetic field which compensates for the external one. Hence, the magnetic field is confined in the crust and can not penetrate into the core but can cross the outer crust surface.

The external magnetic field of a NS, responsible for the spin-down of pulsars and magnetospheric activity, is anchored in the crust (Goldreich and Julian, 1969). The Hall induction equation, instead, governs the crustal magnetic evolution in the crust and *electron MHD* (eMHD) provides us with the tools to study it.

3.1 Magneto-Hydrodynamics

In a magnetized plasma, the equation of motion for electrons and ions (*Euler equation*) reads

$$\frac{\partial \mathbf{v}_l}{\partial t} + (\mathbf{v}_l \cdot \boldsymbol{\nabla})\mathbf{v}_l + \frac{1}{\rho_l}\boldsymbol{\nabla} P_l = -\boldsymbol{\nabla}\Psi + \frac{Z_l e}{m_l^*}\left(\mathbf{E} + \frac{\mathbf{v}_l}{c} \times \mathbf{B}\right) - \sum_k \frac{\mathbf{v}_l - \mathbf{v}_k}{\tau_{lk}} \tag{3.1}$$

where $\mathbf{v}_l$, P_l, ρ_l, Z_l are respectively the velocity, pressure, mass density for each particle l and m_l^* are the effective masses defined in terms of the Fermi momentum and single particle excitation energy $\varepsilon(p)$ as

$$m^* \equiv p_F \left(\frac{\partial\, \varepsilon(p)}{\partial p}\bigg|_{p_F} \right)^{-1} .$$

The right-hand side of the equation (3.1) corresponds to the sum of external forces. The first term is the gradient of the gravitational potential Ψ while the second is the Lorentz force. Finally, the last one represents the frictional forces between different components due to collisions (Goldreich and Reisenegger, 1992). Collisions are characterized through the *relaxation time* τ_{lk}, which is the inverse of the collision frequency.

Using the hydrostatic equilibrium condition

$$\boldsymbol{\nabla} P + \rho \boldsymbol{\nabla}\Psi = 0, \tag{3.2}$$

the pressure term and the gravitational potential gradient simplify in the equation of motion (3.1). The equation of motion can be split into two dynamical equations for the motion of electrons and ions

$$\begin{aligned} n_Z Ze\left(\mathbf{E}+\frac{\mathbf{v}_Z}{c}\times\mathbf{B}\right)-n_Z\frac{m_Z^*}{\tau_{Zn}}\mathbf{v}_Z-n_Z\frac{m_Z^*}{\tau_{Ze}}(\mathbf{v}_Z-\mathbf{v}_e)=0\ ,\\ -n_e e\left(\mathbf{E}+\frac{\mathbf{v}_e}{c}\times\mathbf{B}\right)-n_e\frac{m_e^*}{\tau_{en}}\mathbf{v}_e-n_e\frac{m_e^*}{\tau_{eZ}}(\mathbf{v}_e-\mathbf{v}_Z)=0\ . \end{aligned} \tag{3.3}$$

Inside the neutron star charge neutrality holds, $n_e = Zn_Z$, so the current density is microscopically defined as

$$\mathbf{J}\equiv e(Zn_Z\mathbf{v}_Z-n_e\mathbf{v}_e)=en_e(\mathbf{v}_Z-\mathbf{v}_e)\ . \tag{3.4}$$

Furthermore, the conservation of momentum implies that

$$n_Z\frac{m_Z^*}{\tau_{Ze}}=n_e\frac{m_e^*}{\tau_{eZ}}\ .$$

Hence, combining the two-fluid equations of motion, charge neutrality condition and momentum conservation leads to

$$\frac{\mathbf{J}\times\mathbf{B}}{cn_e}=\frac{m_Z^*}{\tau_{Zn}}\mathbf{v}_Z+\frac{m_e^*}{\tau_{en}}\mathbf{v}_e\equiv\left(\frac{m_Z^*}{\tau_{Zn}}+\frac{m_e^*}{\tau_{en}}\right)\mathbf{v}_{amb} \tag{3.5}$$

where the *ambipolar velocity* $\mathbf{v}_{amb}$ is defined as the weighted mean velocity of the fluid. Interactions between neutrons and electrons are much weaker compared to those between ions and electrons or neutrons. Consequently, the ambipolar velocity is due only to the ion velocity $\mathbf{v}_{amb} = \mathbf{v}_Z$.

3.2 Hall Induction Equation in eMHD

Inside the crust of a neutron star ions constitute the background reference frame, i.e. a component with very large inertia $m_Z^* \to \infty$. Therefore the ions velocity $\mathbf{v}_Z$, the relaxation time τ_{Zn} and also the ambipolar velocity are all zero. Only electrons can move and produce all the crustal current $\mathbf{J} = -en_e\mathbf{v}_e$ (eMHD regime).

Considering the standard static metric (1.18), the Maxwell equations are

$$\begin{aligned} &\boldsymbol{\nabla}\cdot\mathbf{E}=4\pi\rho_q\ , && \frac{1}{c}\frac{\partial\mathbf{E}}{\partial t}=\boldsymbol{\nabla}\times(\mathrm{e}^{\nu}\mathbf{B})-\frac{4\pi}{c}\mathrm{e}^{\nu}\mathbf{J}\ ,\\ &\boldsymbol{\nabla}\cdot\mathbf{B}=0\ , && \frac{1}{c}\frac{\partial\mathbf{B}}{\partial t}=-\boldsymbol{\nabla}\times(\mathrm{e}^{\nu}\mathbf{E})\ . \end{aligned} \tag{3.6}$$

where also $\boldsymbol{\nabla}$ contains the GR corrections (2.3).

The electron velocity can be computed from the relativistic Ampère's law neglecting the displacement current

$$\mathbf{v}_e=-\frac{c\,\mathrm{e}^{-\nu}}{4\pi en_e}\boldsymbol{\nabla}\times(\mathrm{e}^{\nu}\mathbf{B})\ . \tag{3.7}$$

so that the electron equation of motion (3.3) becomes

$$n_e e\left(\mathbf{E}+\frac{\mathbf{v}_e\times\mathbf{B}}{c}\right)+m_e^*n_e\frac{\mathbf{v}_e}{\tau_e}=0 \tag{3.8}$$

where τ_e is the electron relaxation time. Combining the previous equation with the one for the electron velocity (3.7), the electric field is given by

$$\mathbf{E} = \frac{c\,\mathrm{e}^{-\nu}}{4\pi\sigma}\boldsymbol{\nabla}\times(\mathrm{e}^{\nu}\mathbf{B}) + \frac{\mathrm{e}^{-\nu}}{4\pi e n_e}[\boldsymbol{\nabla}\times(\mathrm{e}^{\nu}\mathbf{B})]\times\mathbf{B} \tag{3.9}$$

where σ is the electrical conductivity. By replacing the previous relation inside the last of Maxwell equation (3.6), one obtains the *Hall induction equation*

$$\frac{\partial\mathbf{B}}{\partial t} = -\boldsymbol{\nabla}\times\left[\eta\boldsymbol{\nabla}\times(\mathrm{e}^{\nu}\mathbf{B}) + \frac{c}{4\pi e n_e}\boldsymbol{\nabla}\times(\mathrm{e}^{\nu}\mathbf{B})\times\mathbf{B}\right] \tag{3.10}$$

where the *magnetic diffusivity* η is defined as

$$\eta = \frac{c^2}{4\pi\sigma}\ .$$

The first term on the right-hand side of the induction equation (3.10) describes Ohmic dissipation. Magnetic energy is converted into heat and this heating source is thought to maintain strongly magnetized neutron stars hot longer than the weakly magnetized ones (Page et al., 2000). The second term is the nonlinear Hall term, which has an important role in the evolution of neutron stars with large magnetic fields, $B \gtrsim 10^{14}$ G (Pons and Geppert, 2007). The Hall term dominates for young and middle-aged strongly magnetized stars, $10^3 - 10^5$ yr. As the star cools down, the Ohmic dissipation must be taken into account. However, the Hall term may dominate even for much lower values of the magnetic field strength if the Ohmic time-scale becomes very long (Viganò, 2013). The Hall cascade is a non-dissipative process (Goldreich and Reisenegger, 1992) and it just reconfigures the magnetic field and redistributes magnetic energy, mainly transferring the energy from the larger to the smaller scales, where it is rapidly dissipated due to Ohmic dissipation.

The Hall induction equation can be recast as

$$\frac{\partial\mathbf{B}}{\partial t} = -\boldsymbol{\nabla}\times\eta\left[\boldsymbol{\nabla}\times(\mathrm{e}^{\nu}\mathbf{B}) + \omega_B\tau_e\frac{\boldsymbol{\nabla}\times(\mathrm{e}^{\nu}\mathbf{B})\times\mathbf{B}}{B}\right]\ , \tag{3.11}$$

where the *magnetization parameter* $\omega_B\tau_e$ is useful to compare the relative importance between the two terms on the right-hand side. This form of the induction equation makes explicit that the magnetization parameter $\omega_B\tau_e$ determines the degree of anisotropy in the heat transfer. If $\omega_B\tau_e \ll 1$, the leading term is the Ohmic diffusive term since collisions dominate and the effects of magnetic field on transport properties are negligible. Instead, if $\omega_B\tau_e \gg 1$, the heat transport is anisotropic. The electric currents are squeezed in a smaller volume and the main effect of the Hall term is to allow magnetic energy transfer between poloidal and toroidal components and from large to small scales. For strong toroidal components, the Hall term also leads to the formation of current sheets, i.e. discontinuities in the tangential components of the magnetic field where dissipation is strongly enhanced (Viganò and Pons, 2012).

3.3 Evolution Equations in a NS Crust

For our purposes, we can drop the general-relativistic corrections and use instead non-relativistic eMHD. Since the thickness of the crust is small, the relativistic effects

have limited importance and will not change qualitatively the results. Moreover, for 3D-simulations the inclusion of general-relativistic effects can become computationally quite demanding, in particular when boundary conditions are imposed (section 4.3).

To couple magnetic and thermal evolution, we need to include in the Hall induction equation (3.11) also thermo-electric effects related to the temperature gradient $\boldsymbol{\nabla} T$. Hence, the non-relativistic induction equation, including the thermal coupling effects, is

$$\frac{\partial \mathbf{B}}{\partial t} = -c\boldsymbol{\nabla} \times \left[\boldsymbol{\sigma}^{-1} \cdot \mathbf{J} + \mathbf{G} \cdot \boldsymbol{\nabla} T - \frac{\boldsymbol{\nabla} \mu}{e} \right] \tag{3.12}$$

with $\boldsymbol{\sigma}$ being the electric conductivity tensor (2.24) and μ the electron chemical potential. The electron current is given by $\mathbf{J} = c\boldsymbol{\nabla} \times \mathbf{B}/4\pi$. The thermopower tensor $\mathbf{G}$ is related to the thermal and electric conductivity tensor by Mott relation (Geppert and Wiebicke, 1991)

$$\mathbf{G} = e \frac{\partial \boldsymbol{\sigma}^{-1}}{\partial \mu}\bigg|_T \cdot \boldsymbol{k} \simeq -\frac{\pi^2 k_B^2 T}{e\mu} \delta_{ij} \tag{3.13}$$

where electrons are assumed to be a perfect Fermi gas. The anisotropic part of the thermopower tensor related to the conductivity, the so-called Ettingshausen-Nernst term, is not considered and we keep only the isotropic part responsible for the Biermann battery effect, called the Seebeck term. This is associated to electrons at the Fermi level and can be understood as the entropy dragged along by the flow of electric currents (Ziman, 1972).

The magnetic field evolution is now coupled with the heat equation governing the temperature evolution

$$C_V \frac{\partial T}{\partial t} = -\boldsymbol{\nabla} \cdot \left(T\mathbf{G} \cdot \mathbf{J} - \boldsymbol{k} \cdot \boldsymbol{\nabla} T - \frac{\mu}{e} \mathbf{J} \right) + \mathbf{E} \cdot \mathbf{J} + N_\nu \tag{3.14}$$

where C_V is the heat capacity per unit volume, $\boldsymbol{k}$ is the thermal conductivity (2.21) and N_ν is the neutrino emissivity related to weak processes (2.15). The first term on the right-hand side represents the electron energy flux.

The evolution equations for magnetic field (3.12) and for temperature (3.14) can be recast in terms of typical values of the crust in a strongly magnetized neutron star (*magnetar*). Then each quantity is normalised compared to reference values, i.e. $T_0 = 10^8$ K, $B_0 = 10^{14}$ G, $\mu_0 = 2.9 \times 10^{-5}$ erg and $\tau_0 = 9.9 \times 10^{-19}$ s. We can define four relevant dynamical length scales, the *Debye length*

$$\lambda = \sqrt{\frac{k_B T_0}{4\pi n_0 e^2}} \ , \tag{3.15}$$

with $n_0 \simeq 2.6 \times 10^{34}$ cm^{-3}, the *skin-depth*

$$d = \sqrt{\frac{\mu_0}{4\pi n_0 e^2}} \ , \tag{3.16}$$

the *Larmor radius*

$$L = \frac{\mu_0}{eB_0} \ , \tag{3.17}$$

and finally the *electron mean free path*

$$l = c\tau_0 \ . \tag{3.18}$$

In addition, the radius is scaled with respect to the star radius $R_{NS} = 10$ km and $C_{V0} = k_B n_0$ is the relevant scale for the heat capacity. The neutrino emissivity is expressed in units of $N_\nu^0 = 8\pi e^2 c^2 R^2 \tau_0 / \mu_0 k_B T_0 = 1.3 \times 10^{14}$ erg s^{-1}cm^{-3}.

The induction equation for $\mathbf{B}$ (3.12) and the heat equation for T (3.14) can be recast as

$$\frac{\partial \mathbf{B}}{\partial t} = \mathrm{Se}\, \boldsymbol{\nabla}\left(\frac{1}{\mu}\right) \times \boldsymbol{\nabla} T^2 + \mathrm{Ha} \boldsymbol{\nabla} \times \left[\frac{1}{\mu^3}\mathbf{B} \times (\boldsymbol{\nabla} \times \mathbf{B})\right] - \boldsymbol{\nabla} \times \left(\frac{1}{\tau \mu^2} \boldsymbol{\nabla} \times \mathbf{B}\right) \quad (3.19)$$

$$\frac{1}{\mathrm{Ro}} \frac{C_V}{T} \frac{\partial T^2}{\partial t} = \boldsymbol{\nabla} \cdot (\tau \mu^2 \boldsymbol{\chi} \cdot \boldsymbol{\nabla} T^2) + \frac{\mathrm{Pe}}{\mathrm{Se}} \frac{|\boldsymbol{\nabla} \times \mathbf{B}|^2}{\tau \mu^2} + \mathrm{Pe}\, \mu (\boldsymbol{\nabla} \times \mathbf{B}) \cdot \boldsymbol{\nabla}\left(\frac{T^2}{\mu^2}\right) + \frac{N_\nu}{\mathrm{Ro}} \quad (3.20)$$

where we defined the tensor $\boldsymbol{\chi}$

$$\chi_{ij} = \frac{\delta_{ij} + \mathrm{Ha}^2 (\tau/\mu)^2 B_i B_j - \mathrm{Ha}(\tau/\mu)\epsilon_{ijk} B_k}{1 + \mathrm{Ha}^2 (\tau/\mu)^2 |\mathbf{B}|^2} \quad (3.21)$$

and introduced the following adimensional numbers

$$\begin{aligned}
&\mathrm{Ha} \equiv \frac{l}{L} \simeq 50 && \textit{Hall} \\
&\mathrm{Se} \equiv \frac{\pi^2 L l \lambda^4}{2 d^6} \simeq 0.05 && \textit{Seebeck} \\
&\mathrm{Pe} \equiv \frac{3 d^2}{L l} \simeq 6 \times 10^{-5} && \textit{Peclet} \\
&\frac{1}{\mathrm{Ro}} \equiv \sqrt{\frac{3}{2\pi^2} \frac{\mathrm{Pe}}{\mathrm{SeHa}^2}} \simeq 3 \times 10^{-4} && \textit{Roberts.}
\end{aligned}$$

If we also assume $C_V = \tau \mu^2 T$ to have the thermal diffusivity constant over the whole domain, the heat equation (3.20) becomes a differential equation depending on temperature only through T^2. This results in a great advantage for the efficiency of the numerical implementation (Chapter 4). However, this assumption holds only for the electron contribution and not the lattice contribution. Nevertheless, this term is negligible in most situations, since it is suppressed by a large factor 1/Ro, so that this assumption is reasonable when studying magnetic dominated evolution.

In the eMHD approximation, the time-independent number density for electrons and protons in the crust is the same. Since we assume that the crust is spherically symmetric, n is a function of the radius r only. Furthermore, we need to specify explicit relations for μ and τ. For simplicity, we can assume that both are independent on temperature and depend on r alone. We consider the realistic profile used in Gourgouliatos and Cumming (2013)

$$\mu = \left(1 + \frac{1 - r}{0.0463}\right)^{4/3} \quad \text{and} \quad \tau = 1\ . \quad (3.22)$$

These profiles are only rough approximations to the (highly uncertain) profiles in real neutron stars but are good analytical fits at temperatures $\approx 10^8$ K (Gourgouliatos et al., 2016). The assumption that the relaxation rate τ is independent of temperature holds well in the lower crust where scattering by impurities dominates, while it is just an approximation in the upper crust, where scattering by mostly by phonons (Potekhin et al., 2015).

The relevant timescales for the magnetic evolution are the Hall and Ohm ones defined as

$$\tau_H = \frac{4\pi n_0 e L^2}{c B_0} \approx 10^4 \text{ yr} , \tag{3.23}$$

$$\tau_O = \frac{4\pi \sigma_0 L^2}{c^2} \approx 10^7 \text{ yr} . \tag{3.24}$$

On the Hall timescale, magnetic field reconfiguration takes place and small scale structures are formed by the action of the Hall term. Dissipation occurs on the Ohm timescale. The ratio between the two timescales is simply the magnetization parameter $\omega_B \tau$ (3.11). Long-term thermal evolution also occurs on timescale $\lesssim \tau_O$.

3.4 Poloidal-Toroidal decomposition

In the numerical simulations, the initial conditions are given in term of *poloidal* and *toroidal* components of magnetic field. Any three-dimensional, solenoidal vector field $\mathbf{B}$ can be expressed in terms of poloidal and toroidal components

$$\mathbf{B} = \mathbf{B}_{\text{pol}} + \mathbf{B}_{\text{tor}} . \tag{3.25}$$

The two component can be defined in terms of two scalar functions $\Phi(\mathbf{r}, t)$ and $\Psi(\mathbf{r}, t)$ as follows

$$\begin{aligned} \mathbf{B}_{\text{pol}} &= \boldsymbol{\nabla} \times [\boldsymbol{\nabla} \times (\Phi \mathbf{k})] , \\ \mathbf{B}_{\text{tor}} &= \boldsymbol{\nabla} \times (\Psi \mathbf{k}) , \end{aligned} \tag{3.26}$$

where $\mathbf{k}$ is an arbitrary vector. Using spherical coordinates (r, θ, φ), the suitable choice is $\mathbf{k} = \mathbf{r}$ and, since $\boldsymbol{\nabla} \times \mathbf{r} = 0$, we can rewrite

$$\begin{aligned} \mathbf{B}_{\text{pol}} &= \boldsymbol{\nabla} \times (\boldsymbol{\nabla} \Phi \times \mathbf{r}) , \\ \mathbf{B}_{\text{tor}} &= \boldsymbol{\nabla} \Psi \times \mathbf{r} . \end{aligned} \tag{3.27}$$

For axial symmetry with respect to the $\hat{z}$ axis, the two scalar functions depend only on r and θ and the toroidal magnetic field is directed along the azimuthal direction φ. Alternatively, the poloidal component can be recast in terms of the *magnetic flux function* Γ

$$\mathbf{B} = \frac{\boldsymbol{\nabla} \Gamma(r, \theta) \times \hat{\boldsymbol{e}}_\varphi}{r \sin \theta} + B_t(r, \theta) \hat{\boldsymbol{e}}_\varphi . \tag{3.28}$$

4. Numerical Implementation

Numerical simulations are essential to solve the magnetic evolution equation (3.19) together with the heat equation (3.20). To this end we used a version of PARODY, a pseudo-spectral and parallel 3D code, originally developed by Dormy et al. (1998) and Aubert et al. (2008), suitably modified to include the NS evolution equations and boundary conditions (Wood and Hollerbach, 2015).

4.1 Spectral Decomposition

Spherical harmonics provide the basis for spectral decomposition in our algorithm. The angular part of all the quantities are decomposed in term of spherical harmonics Y_l^m

$$T(\theta,\phi) = \sum_{l=0}^{\infty} \sum_{m=-l}^{+l} T_{lm} Y_l^m(\theta,\phi) \ . \tag{4.1}$$

The expansion coefficients are

$$T_{lm} = \int_{4\pi} T(\theta,\phi)\, Y_{lm}^*(\theta,\phi) d\Omega \tag{4.2}$$

where we integrate over $d\Omega = \sin\theta d\theta d\phi$. Spherical harmonics are a set of complex functions defined over the sphere

$$Y_l^m(\theta,\phi) = C_l^m P_l^m(\cos\theta)\, \mathrm{e}^{im\phi} \tag{4.3}$$

with C_l^m a normalization constant and P_l^m the associated Legendre polynomial of degree l and order m defined as

$$P_l^m(x) = (-1)^m (1-x^2)^{m/2} \frac{d^m}{dx^m} P_l(x) \tag{4.4}$$

where $P_l(x)$ is the Legendre polynomial of degree l (see Appendix A.1). The normalization factor is chosen as

$$C_l^m = \sqrt{(2-\delta_{m0})(2l+1)\frac{(l-m)!}{(l+m)!}} \tag{4.5}$$

to have normalized spherical harmonics,

$$\int_{-\pi}^{\pi} \int_{0}^{\pi} Y_l^m(\theta,\phi)^*\, Y_{l'}^{m'}(\theta,\phi) \sin\theta\, d\theta\, d\phi = 4\pi \delta_{ll'} \delta_{mm'} \tag{4.6}$$

with δ_{ij} being the Knonecker delta.

4.2 Spectral Algorithms

PARODY is a pseudo-spectral meaning that it treats the radial part of the differential operators by means of a finite-difference scheme grid while for the angular part a spectral decomposition is used. Spectral algorithms are a class of methods to solve partial differential equations (PDEs) in which the solution of the equations is written as a sum of certain basis function, such as the spherical harmonics, and the coefficients in the sum are chosen to satisfy the PDEs.

The time-stepping algorithm is Crank-Nicholson for the Ohmic diffusion, backward-Euler for the isotropic part of the thermal diffusion, and Adams-Bashforth for all other terms. The Crank-Nicholson algorithm is a finite difference method used for numerically solving partial differential equations, such as the heat equation. This method is based on the trapezoidal rule giving second-order convergence in time and its equation is a combination of the forward Euler method at step n and the backward Euler method at $n+1$. The Adam-Bashfort algorithm is an explicit linear multistep method used to numerically solve ordinary differential equations based on the idea of approximating the integrand with a polynomial within the time interval.

In explicit algorithms to solve PDEs involving propagating waves, the time step is limited by the Courant condition, which essentially states that waves cannot travel more than one cell length on each time step, avoiding numerical instabilities. The time step is computed in an adaptive way using a Courant condition preserving method.

The angular grid is of Gauss-Legendre type in colatitude θ and longitude ϕ, whereas the radial grid is uniformly spaced in radius r. The Gauss-Legendre grid is characterized by gridpoints equally spaced in latitude while spacing of latitudes at each longitude is dbased on Gaussian quadrature points so gridpoints along each longitude are not equally spaced. The spatial resolution of the code in the two dimensions orthogonal to r depends on the adopted number of modes, l and m. Using $\approx$ 100-modes, a typical resolution of ≈ 100 m is obtained on the surface. The code is run on a cluster of CPUs at CloudVeneto, a high performance computing (HPC) facility jointly owned by the University of Padova and INFN, using also parallelisation with MPI.

4.3 Boundary Conditions

The solution of the Hall induction equation (3.12) combined with the temperature evolution equation (3.14) requires some boundary conditions at the core-crust interface and at the outer crust surface.

As for the temperature, the thermal evolution of the NS core determines the boundary condition between core and crust. Assuming an isothermal cooling model (see chapter 2) for the core, the evolution of the crust-core temperature T_{cc} due to neutrino emission is obtained solving the equation

$$\frac{\partial T_{cc}}{\partial t} = -\frac{N_c(T)}{C_c} \tag{4.7}$$

where C_c is the specific heat of the core while $N_c(T) = N_c T^k$ is the core neutrino emissivity. In particular, the code assumes a standard, slow-cooling model with $k = 8$, $C_c = 10^{20}$ erg s^{-1} K^{-2} and $N_c = 10^{21}$ erg cm^{-3} K^{-8} (Page et al., 2004).

The surface temperature is controlled by the properties of the thermal blanketing envelope. The equation linking the surface temperature T_s with the temperature

gradient in the envelope has been already introduced in section (2.2) and it serves as the second boundary condition for temperature.

All magnetic flux is expelled from the superconducting core since we have considered a Type-I superconducting core (*Meissner condition*). This requires that the normal component of the magnetic field and tangential electric field must vanish at the core-crust interface $r = r_c$. The previous condition results in a non-linear boundary condition for the magnetic field due to the presence of the Hall term Since near the crust-core interface the electron density is high, the contribution of the non-linear term is negligible (Hollerbach and Rüdiger, 2004). So that, the boundary conditions can be written in terms of the radial magnetic field and tangential current:

$$B_r(r_c) = 0 \qquad J_t(r_c) = 0 \ . \tag{4.8}$$

This is a simplifying assumption, as the core may be a Type-II superconductor and magnetically coupled to the crust.

The magnetic currents in the magnetosphere are negligible compared to those in the crust, so the magnetic field is irrotational at the outer crust boundary

$$\boldsymbol{\nabla} \times \mathbf{B}|_{R_{NS}} = 0 \ . \tag{4.9}$$

This can be achieved in a very natural way by exploiting the spectral nature of our code, using the poloidal-toroidal decomposition (3.26) and spherical harmonics $Y_l^m(\theta, \phi)$ as the basis (section 4.1). In this representation, each mode of a potential field is purely poloidal and such that $\Phi_l^m \propto r^{-(l+1)}$. Therefore, the boundary conditions is given by

$$\left.\frac{\partial \Phi_l^m}{\partial r} + \frac{l+1}{r}\Phi_l^m\right|_{R_{NS}} = 0 \qquad \Psi_l^m|_{R_{NS}} = 0 \ . \tag{4.10}$$

4.4 Initial Conditions

The initial temperature profile is considered to be a function of radius only and, in particular, it is taken to be a constant, $T(r, t = 0) \equiv 1 \times 10^8$ K. This translates into a monopole distribution in the spherical harmonics space. However, the overall evolution is virtually independent on this choice inasmuch as the first term in the temperature equation (3.14) is suppressed by a factor $\mathrm{Ro}^{-1} \approx 10^{-4}$. So the magnetic evolution drives the thermal one and this quickly washes out the initial condition.

In order to set the initial magnetic configuration for our simulations, we followed the widespread approach (see e.g. Rüdiger and Hollerbach, 2005), to start with some large-scale field and study the subsequent evolution. In particular we chose solutions of the force-free equation as initial conditions.

From the standard magneto-hydrodynamics equation (3.1) assuming no collisions and that pressure force are negligible with respect to the Lorentz one, we can recover the force-free equation

$$(\boldsymbol{\nabla} \times \mathbf{B}) \times \mathbf{B} = 0 \ . \tag{4.11}$$

This implies that

$$\boldsymbol{\nabla} \times \mathbf{B} = \alpha(r, \theta)\mathbf{B} \tag{4.12}$$

where, a priori, the proportionality factor α is a generic function of the position. Inserting the general expression for an axisymmetric field (3.28) into the force-free condition (4.11), one obtains two independent scalar equations for the toroidal

component B_t and the flux function Γ. The first one for the toroidal part is

$$B_t(r,\theta) = \frac{1}{r\sin\theta}F(\Gamma) \tag{4.13}$$

where F is an arbitrary function of Γ only (Low and Lou, 1990). Combining the previous relation with the one for the magnetic flux, leads to the Grad-Schlüter-Shafranov (GSS) equation (see e.g. Pavan et al., 2009)

$$\frac{\partial^2\Gamma}{\partial r^2} + \frac{1-\mu^2}{r^2}\frac{\partial^2\Gamma}{\partial\mu^2} + F(\Gamma)\frac{dF}{d\Gamma} = 0 \tag{4.14}$$

with $\mu = \cos\theta$. The GSS equation can be reduced to an ordinary differential equation by making suitable assumptions on the dependence of Γ on the coordinates.

Using spherical polar coordinates (r,θ,ϕ) and spherical harmonics decomposition, the magnetic field satisfiyng the force-free equation is

$$\mathbf{B} = \sum_{l=0}^{\infty}\sum_{m=-l}^{+l} Y_l^m(\theta,\phi)\mathbf{B}_{lm} \tag{4.15}$$

where $\mathbf{B}_{lm}$ is the sum of a poloidal field $\mathbf{B}^{\rm pol}_{lm}$ and a toroidal field $\mathbf{B}^{\rm tor}_{lm}$. Indeed, given any poloidal field, we can find a toroidal field $\mathbf{B}^{\rm tor}$ which, when added to $\mathbf{B}^{\rm pol}$ makes the total field force-free and viceversa.

From (3.26) fixing $\mathbf{k} = r\hat{\mathbf{e}}_r$, the two components can be derived as (Chandrasekhar and Kendall, 1957)

$$\mathbf{B}^{\rm pol}_{lm} = \left[\frac{l(l+1)}{\alpha r}Z_l(\alpha r)Y_l^m(\theta,\phi)\right]\hat{\mathbf{e}}_r + \left\{\frac{1}{\alpha r}C_l^m e^{im\phi}\frac{\partial}{\partial\theta}P_l^m(\cos\theta)\frac{\partial}{\partial r}\left[r^2 Z_l(\alpha r)\right]\right\}\hat{\mathbf{e}}_\theta + \left\{\frac{m}{\alpha\sin\theta}Y_l^m(\theta,\phi)\frac{\partial}{\partial r}\left[rZ_l(\alpha r)\right]\right\}\hat{\mathbf{e}}_\phi \tag{4.16}$$

and

$$\mathbf{B}^{\rm tor}_{lm} = \left[\frac{m}{\sin\theta}\psi_l^m(r,\theta,\phi)\right]\hat{\mathbf{e}}_\theta - \left[Z_l(\alpha r)C_l^m e^{im\phi}\frac{\partial}{\partial\theta}P_l^m(\cos\theta)\right]\hat{\mathbf{e}}_\phi \tag{4.17}$$

where ψ_l^m are a set of fundamental solutions of scalar Helmholtz equation

$$\nabla^2\psi + \alpha^2\psi = 0 \tag{4.18}$$

where are given by

$$\psi_l^m(r,\theta,\phi) = Z_l(\alpha r)Y_l^m(\theta,\phi) \tag{4.19}$$

and $Z_l(\alpha r)$ is a linear combination of the spherical Bessel functions $j_l(\alpha r)$ and $y_l(\alpha r)$ (see Appendix A.2)

$$Z_l(\alpha r) = a_l j_l(\alpha r) + b_l y_l(\alpha r) \tag{4.20}$$

where the coefficients a_l and b_l are constants determined by the boundary conditions.

The previous relations for poloidal (4.16) and toroidal (4.17) components, provide us the tools to set multipolar and/or non-axisymmetric initial configuration for the magnetic field since the code requires initial conditions in spherical harmonics space.

5. Numerical 3D Simulations

We present now the results of 3D numerical simulations of coupled magneto-thermal evolution of isolated neutron stars starting from a range of different initial conditions for the magnetic field. First, we deal with axisymmetric configuration to have a better comparison with previous works (Viganò et al., 2013). This axisymmetric cases tend to maintain their symmetry during the long-term evolution.

Then, our focus will be on initial configurations that allow us to fully exploit the three-dimensionality of our code and, in particular, we consider the case of a dipolar field tilted with respect to a quadrupolar component. These are non-axisymmetric configurations for which 3D maps of magnetic field and temperature are necessary to analize the NS evolution.

5.1 Axisymmetric Configurations

The first configuration taken into consideration is a pure dipolar field. Its evolution is followed for about $t \approx 10^4$ yr $\approx \tau_H$ to compute the magnetic field components and the temperature map of the crust and the NS surface.

Then we show that, after a few Hall timescale, the dipole initial field (and also a more general one considering a toroidal component) evolves towards a configuration dominated by odd modes. So this solution, the so-called *Hall attractor*, can be considered as the initial condition to follow the late-stage evolution of a NS.

5.1.1 Dipole Configuration

After a Hall timescale the magnetic field tends to exhibit an equatorial structure where the field is stronger (Gourgouliatos et al., 2016) and small scale structures due to the effect of the Hall term. This can be seen in Figure 5.1, showing the magnetic field spherical components B_r, B_θ and B_ϕ at the beginning of the simulation and after $t \simeq 5 \times 10^4$ yr for an initial configuration with $B_{\rm pol}(0) \approx 10^{13}$ G. Since there is no initial toroidal field, $B_t(0) = 0$, there is no B_ϕ component at the beginnig of the run so the last plot (Figure 5.1, top right) displays the field lines of the magnetic topology.

According to the Hall induction equation (3.12), the poloidal field will immediately induce a toroidal field as well, which, according to the symmetry properties discussed in Hollerbach and Rüdiger (2002), will have the same equatorial symmetry as the case of a toroidal quadrupole. So we expect that a toroidal field is very rapidly induced, and immediately starts "compressing" the poloidal field into the equatorial region in which the field is stronger. The maximum amplitude of this induced toroidal field rapidly increases then gradually decays. It turns out that the sign of this field is negative/positive in the northern/southern hemisphere. The equatorial structure related to the appearance of a strong toroidal component reflects into a

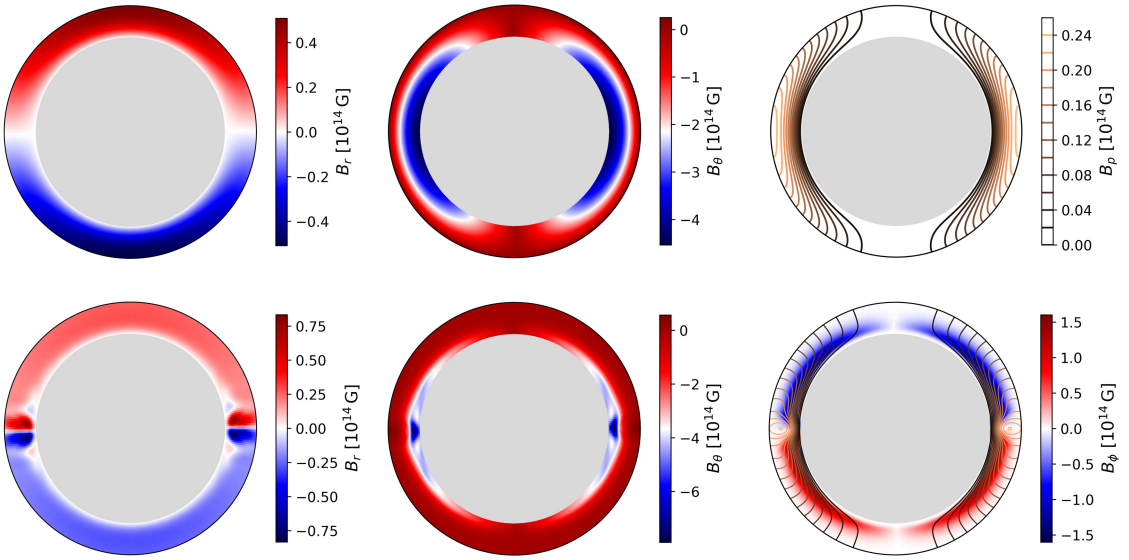

Figure 5.1: Meridional cuts of the crust along the prime meridian ($\phi = 0$) displaying the magnetic field components B_r, B_θ and B_ϕ (from left to right) at the beginning of our simulation (top row) and after 5×10^4 yr $\approx \tau_H$ (bottom row) for an initial configuration characterized by $B_p(0) \approx 10^{13}$ G (the thickness of the crust is 4 times stretched for better visualization).

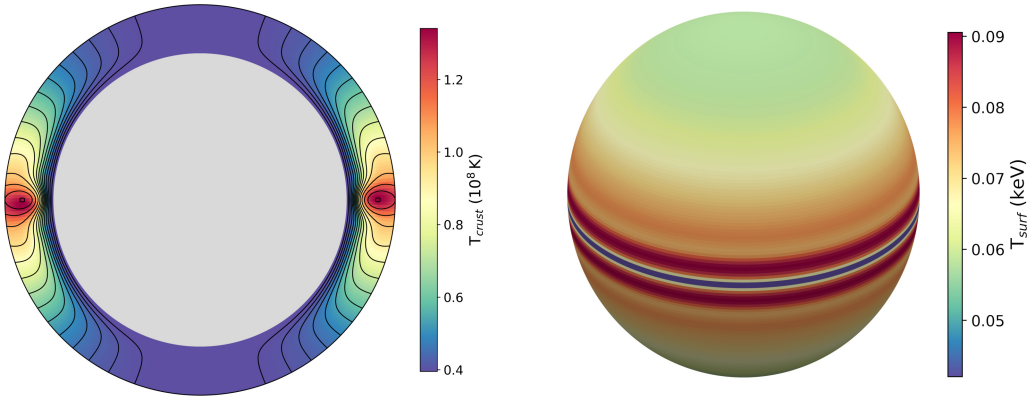

Figure 5.2: Temperature maps after $t \simeq 5 \times 10^4$ yr $\approx \tau_H$ for a case with $B_p(0) \approx 10^{13}$ G. On the left, the meridional cut is shown with the magnetic field lines while, on the right, the temperature map of the NS surface is displayed (the thickness of the crust is 4 times stretched for better visualization).

hotter equatorial region in the temperature distribution (Figure 5.2, left panel), according to the magnetic evolution drives the thermal one.

Moreover, for equation (2.23) heat tends to be transported along the field lines so that the equatorial region is hotter not only because of higher dissipation, but also because heat is trapped by the closed field lines appearing in that region. The surface temperature map (Figure 5.2, right panel) is derived using the Tsuruta law (2.11) to take into account the properties of the heat blanketing envelope. The overall topology of the two maps is quite different: the equatorial region shows a colder ring surrounded by a hotter belt.

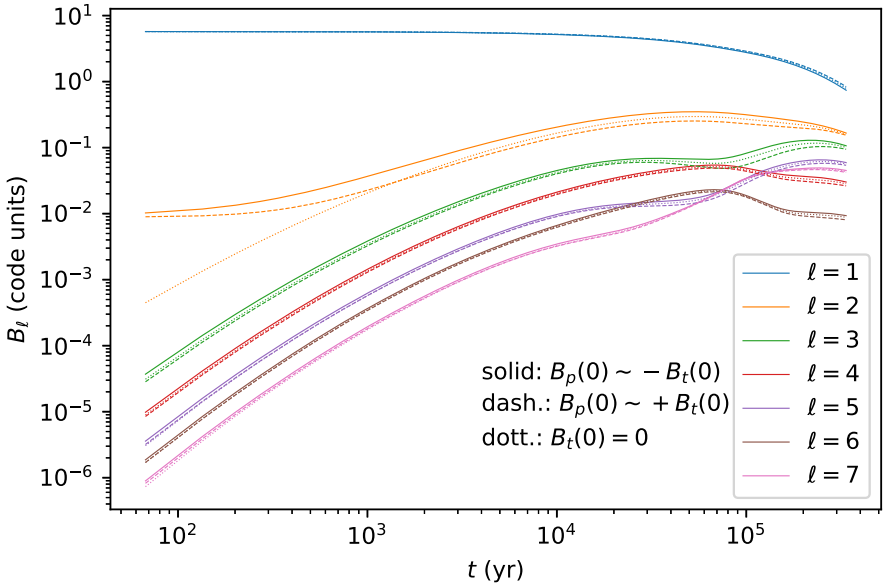

Figure 5.3: Time evolution of the first seven l modes for three different initial magnetic field configurations: a purely poloidal field (solid) and two cases with an added toroidal field of opposite polarity (dashed and dotted).

5.1.2 Hall Attractor

The Hall term in the magnetic evolution equation (3.12) will transfer energy between poloidal and toroidal components, so that, even by assuming an initial we assumed a purely poloidal field, a toroidal component will appear during the evolution and viceversa. Considering three different initial magnetic configurations, a purely poloidal field ($B_t(0) = 0$) and a field with poloidal and toroidal components of the same order but opposite polarity ($B_p(0) \sim \pm B_t(0)$), the magnetic evolution can be followed over a few Hall timescale (De Grandis et al., 2020). The code, indeed, provides us the values of the magnetic energy U_l step by step for the first seven l-modes. Figure 5.3 shows the magnetic energy spectrum as function of time and in all our cases the magnetic field evolves towards a configuration dominated by the modes $l = 1, 2, 3, 5, 7$. This is a general feature of the so-called *Hall attractor* (Gourgouliatos and Cumming, 2014).

After a few τ_H, under the assumption of axial symmetry, the Hall evolution saturates and the magnetic field relaxes to a particular stable configuration which is insensitive to the choice of initial conditions. This consists of a dipole component ($l = 1$) and an octupole ($l = 3$) whose relative intensity depends on the crust properties, and is counter-aligned with the dipole. Higher multipoles are present, but their intensity is smaller. The weak toroidal field developed is in the $l = 2$ component and is responsible for the transfer of energy from the dipole poloidal component into the octupole to compensate for the losses due to dissipation. This evolution is an advection-diffusion equilibrium where the system maintains its structure and evolves self-similarly in time, with energy dissipation related to the Ohmic term and the slightly imbalanced Hall term rearranging the field so that the changes in the structure are annulled. Once a NS reaches the attractor stage, it will spend about a Myr of its life in this state, until the field has dissipated so much that the Ohmic timescale is comparable with the Hall one and the successive evolution is driven mainly by the relatively slow Ohmic dissipation. Then higher multipoles dissipate faster with the dipole surviving the longest.

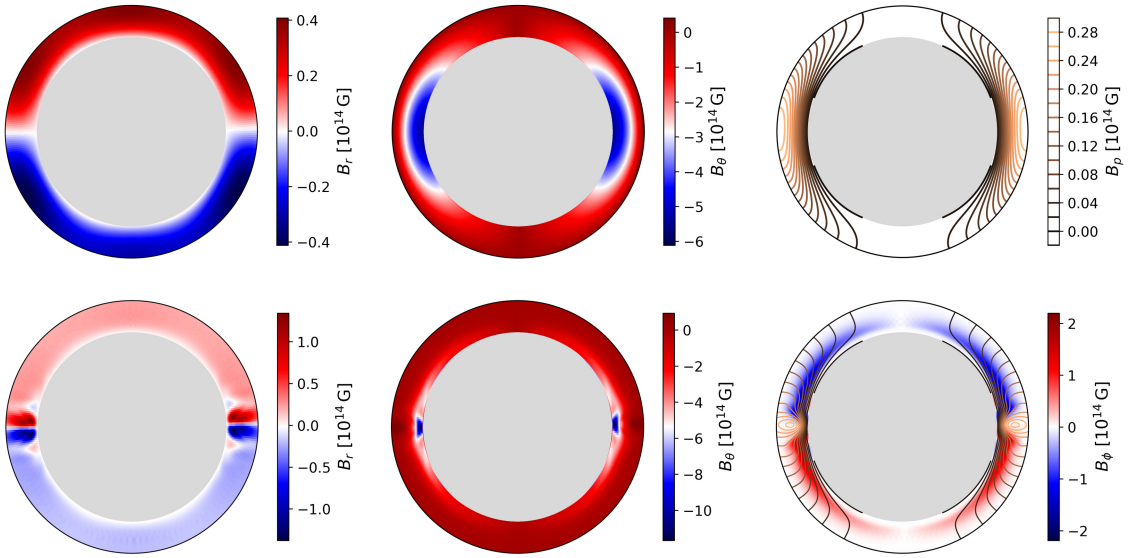

Figure 5.4: Meridional cuts of the crust along the prime meridian ($\phi = 0$) displaying the magnetic field components B_r, B_θ and B_ϕ (from left to right) at the beginning of our simulation (top row) and after 5×10^4 yr $\approx \tau_H$ (bottom row) for an initial configuration with $l = 1, 2, 3, 5$ modes for the poloidal component (the thickness of the crust is 4 times stretched for better visualization).

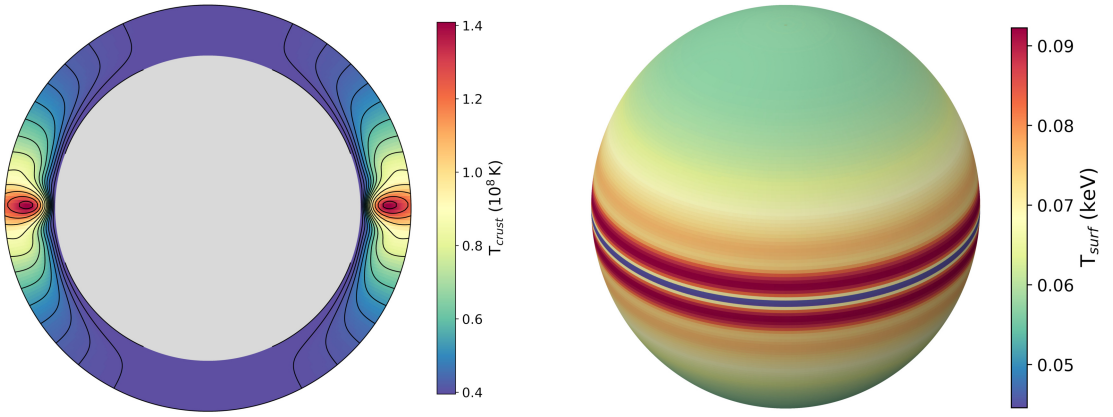

Figure 5.5: Temperature maps after $t \simeq 5 \times 10^4$ yr $\approx \tau_H$ for an Hall attractor case. On the left, the meridional cut is shown with the magnetic field lines while, on the right, the temperature map of the NS surface is displayed (the thickness of the crust is 4 times stretched for better visualization).

Following Gourgouliatos and Cumming (2013), we mimicked the Hall attractor stage as initial condition adopting a magnetic field topology with $l = 1, 2, 3, 5$ modes for the poloidal component. In particular, we consider a combination of dipolar and octupolar components with opposite polarity and polar ratio $\rho_3 = 0.6$, with the addition of a small quadrupolar field with $\rho_2 = 0.1$ and an $l = 5$ component characterized by $\rho_5 = 0.3$. According to the measured values of P and $\dot{P}$ for the neutron star RX J1856.5-3754 taken into consideration by Popov et al. (2016), we set the magnetic field intensity for the dipolar component at the poles at $B_{\rm dip} \simeq 5 \times 10^{13}$ G.

A toroidal fiels is immediately induced by the poloidal components according to the Hall equation (3.12) and will grow up as the magnetic field evolves in time reaching values of about 10^{14} G at $t \approx 5 \times 10^4$ yr. The radial component of the magnetic field B_r tend decreases during the NS evolution except in the equatorial

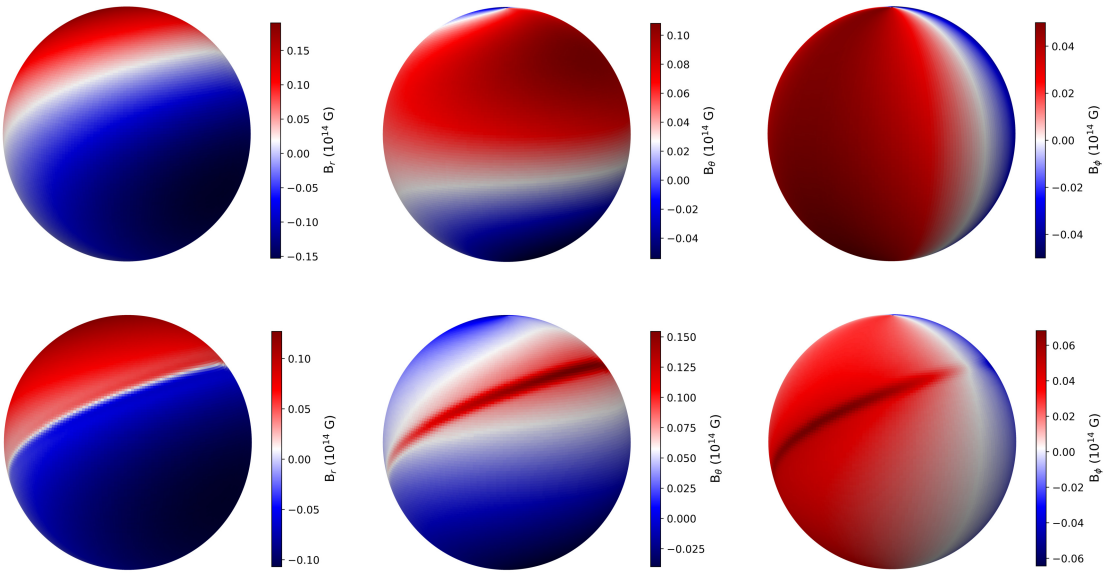

Figure 5.6: Maps displaying the magnetic field components B_r, B_θ and B_ϕ (from left to right) at the top of the crust, at the beginning of our simulation (top row) and after 5×10^4 yr $\approx \tau_H$ (bottom row) for a run with $B_{\rm Dip}(0) \simeq 10^{13}$ G tilted by $\Theta_B = 45°$ with respect to $B_{\rm Quad}(0) \simeq 7.5 \times 10^{12}$ G (run45B0.75).

Run Tag	$B_{\rm Dip}(0)$	$B_{\rm Quad}(0)$	β_B	Θ_B
run45B0.75	10^{13} G	7.5×10^{12} G	0.75	45°
run45B1.25	10^{13} G	1.25×10^{13} G	1.25	45°
run45B10	10^{13} G	10^{14} G	10	45°
run90B1	10^{13} G	10^{13} G	1	90°

Table 5.1: Tags, initial magnetic field values and the disalignment angle Θ_B of the simulations in section 5.2 characterized by non-axisymmetric configuration of the magnetic topology.

region where the field is stronger. Furthermore, the initial configuration of B_r is quite similar to the dipole one but two parallel structures, related to higher multipoles, in which the magnetic field is slightly stronger can be highlighted near the outer crust at latitude $\approx 25°$, one in each hemisphere. Temperature maps are shown in Figure 5.5 and the equatorial hotter region related to the strong toroidal component is clearly evident as in the case of a pure dipole field. Both temperature maps are quite similar to the one of the dipole configuration (Figure 5.2) as we expect, since all the magnetic field configurations evolve toward the Hall attractor stage. The surface temperature map exhibits the same cold equatorial ring with nearby hotter regions.

5.2 Non-Axisymmetric Configuration

We can now turn to the study non-axisymmetric cases. Recently, Kondratyev et al. (2020) (KON20 hereafter) proposed a field configuration made of a dipole and a quadrupole with misaligned axes in order to explain observations of non-symmetric pulse profile and amplified pulsations in comparison to the pure-dipolar case. The non-coaxial dipole and quadrupole magnetic configuration, indeed, can significantly affect the thermal light curve, amplifying the pulsations and making the pulse profile

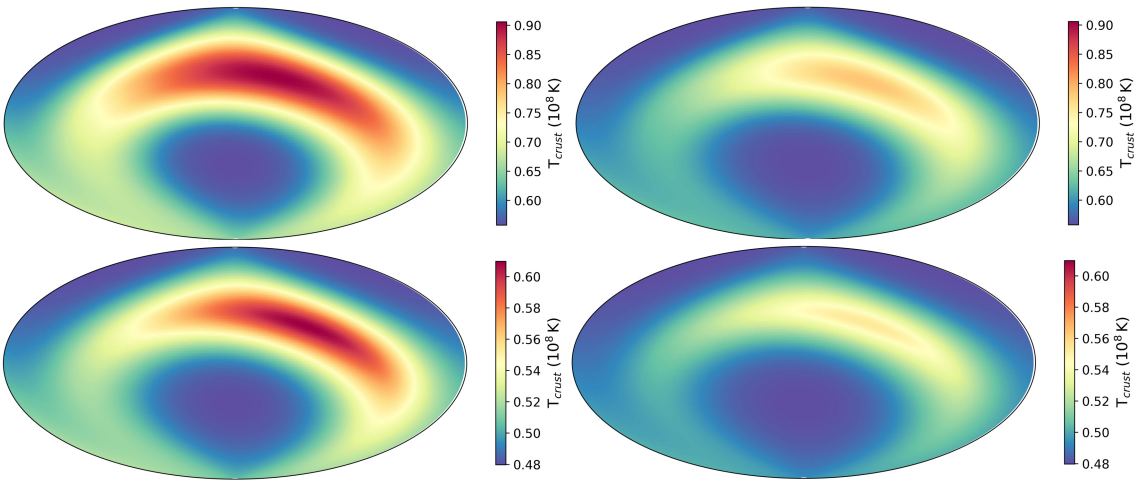

Figure 5.7: Evolution of the temperature (Mollweide projection) at the top of the crust for run45B0.75, see Table 5.1. Time increases from left to right and from top to bottom. Snapshots are separated by $\approx$ 6000 yr and the first one (top left) is at $t \approx 6000$ yr. Note that the colour bar range decreases between the top and the bottom row to improve visualisation.

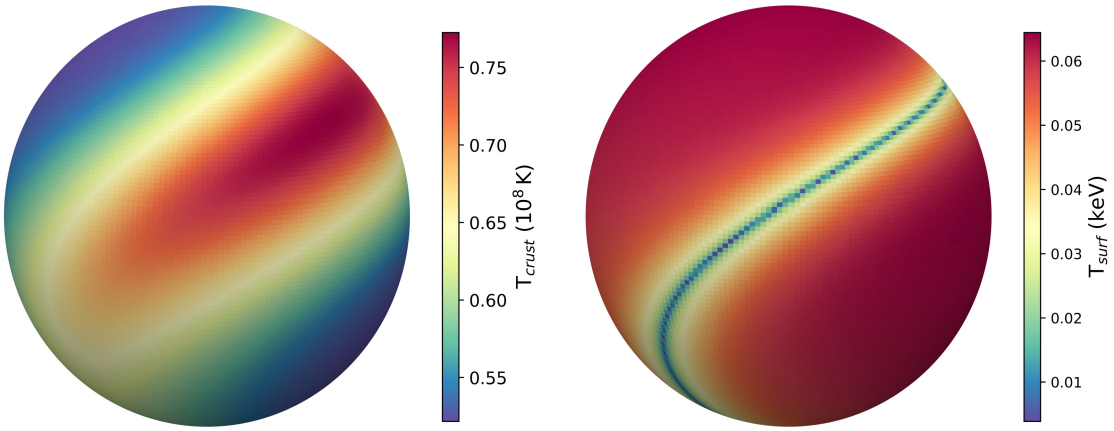

Figure 5.8: Temperature maps at the top of the crust (left) and on the NS surface (right) after $t \simeq 10^4$ yr for the same run as in Figure 5.7 (run45B0.75).

asymmetric with respect to the pure-dipolar case. However, their model relied on a stationary state approximation for crustal temperature given a fixed magnetic field. We extend this work using a "tilted" configuration as an initial condition, and then following its evolution consistently. Furthermore, since our simulations provide the evolution of the magnetic field, we can check how the angle between the two components evolves to see if they tend to realign with each other or the initial configuration is maintained.

Following KON20, we describe our magnetic field configuration by two parameters Θ_B, which corresponds to the angle between the dipolar and quadrupolar component, and $\beta_B = B_{\rm Quad}/B_{\rm Dip}$ describing the strength of the quadrupolar component with respect to the dipole. Consequently, if $\beta_B \ll 1$ then the temperature approaches to a pure dipolar configurations, while if $\beta_B \gg 1$ a pure-quadrupolar one will be observable. In order to set an initial magnetic configuration rotated with respect to an axis, a tool to rotate spherical harmonics is required. Under a generic rotation $\Lambda(\alpha, \beta, \gamma)$ where α, β and γ are the Euler angles, each spherical harmonic is transformed into a linear combination of Y_l^n with $-l \leq n \leq l$ and same degree l

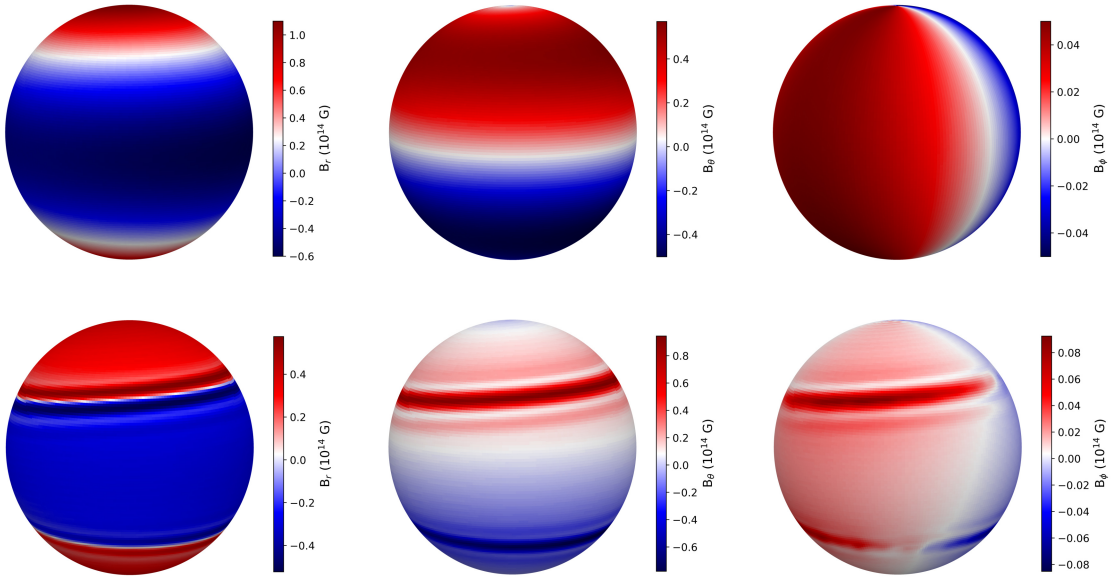

Figure 5.9: Maps displaying the magnetic field components B_r, B_θ and B_ϕ (from left to right) at the top of the crust, at the beginning of our simulation (top row) and after 5×10^4 yr $\approx \tau_H$ (bottom row) for run45B10, see Table 5.1.

(Driscoll and Healy, 1994):

$$\Lambda(\alpha, \beta, \gamma) Y_l^m(\theta, \phi) = \sum_{n=-l}^{l} Y_l^n(\theta, \phi) D_{nm}^{(l)}(\alpha, \beta, \gamma) \ . \tag{5.1}$$

Here $D^{(l)}$ is an irreducible representation of the group SO(3), the so-called *Wigner matrix*, and can be written as:

$$D_{nm}^{(l)}(\alpha, \beta, \gamma) = \mathrm{e}^{-in\gamma} \, d_{nm}^{(l)}(\cos\beta) \, \mathrm{e}^{-im\alpha} \ , \tag{5.2}$$

where $d_{nm}^{(l)}$ are related to Jacobi Polynomials (see Appendix A.3). Hence the effect of a rotation is expressed in the basis of spherical harmonics as a product with a semi-infinite block diagonal matrix, with the $(2l+1) \times (2l+1)$ blocks for each $l \geq 0$. This procedure allows us to start from tilted initial conditions after evaluating numerically the coefficients of the rotation matrix.

For our simulations, the initial temperature profile is assumed to be a constant, $T(0) = 10^8$ K and the initial magnetic configuration consists in a dipole field rotated by Θ_B with respect to a quadrupolar component which is directed along the z-axis. We consider an initial dipole $B_{\rm Dip}(0) \simeq 10^{13}$ G and different values of $B_{\rm Quad}(0)$ as shown in Table 5.1 where some values of β_B are chosen to have a direct comparison with the field configurations studied by KON20.

The magnetic field components B_r, B_θ and B_ϕ at the top of the crust are shown in Figure 5.6 at the beginning and after $t \simeq 5 \times 10^4$ yr for the first run (run45B0.75). Note that, in this case, even if we started from a purely poloidal configuration made up of a dipole and a quadrupole, the ϕ-component is not vanishing since the field is no more axisymmetric. As in the axisymmetric case, the radial component decreases in time since its energy is transferred to the other components and the region with inversion of polarity becomes thinner. Moreover, due to the Hall term (3.12), some structures in which the magnetic field is stronger are visibile in both B_θ and B_ϕ maps at colatitude $\approx \pi - \Theta_B$.

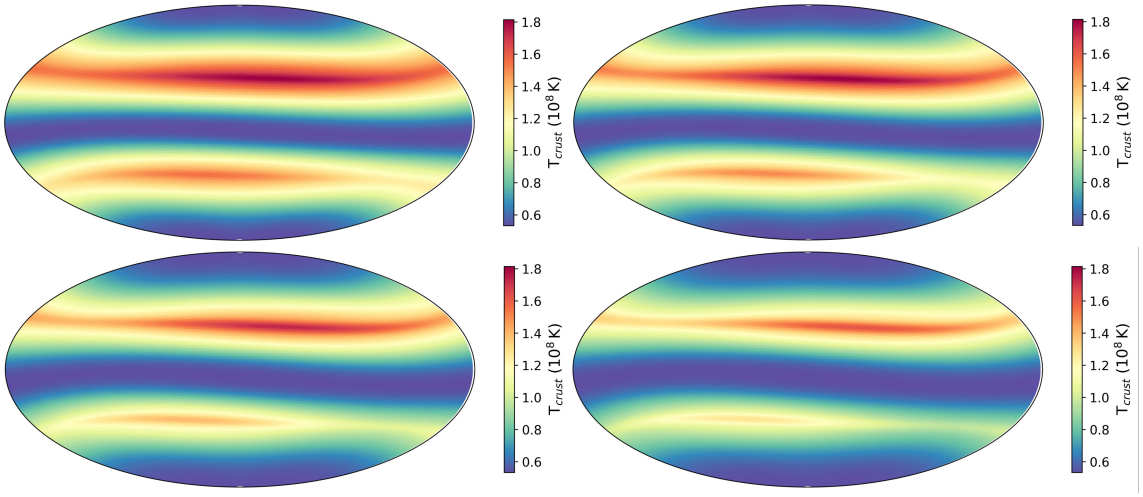

Figure 5.10: Evolution of the temperature (Mollweide projection) at the top of the crust for the same run as in Figure 5.6 (run45B10). Time increases from left to right and from top to bottom. Snapshots are separated by $\approx$ 5000 yr and the first one (top left) is at $t \approx 6000$ yr.

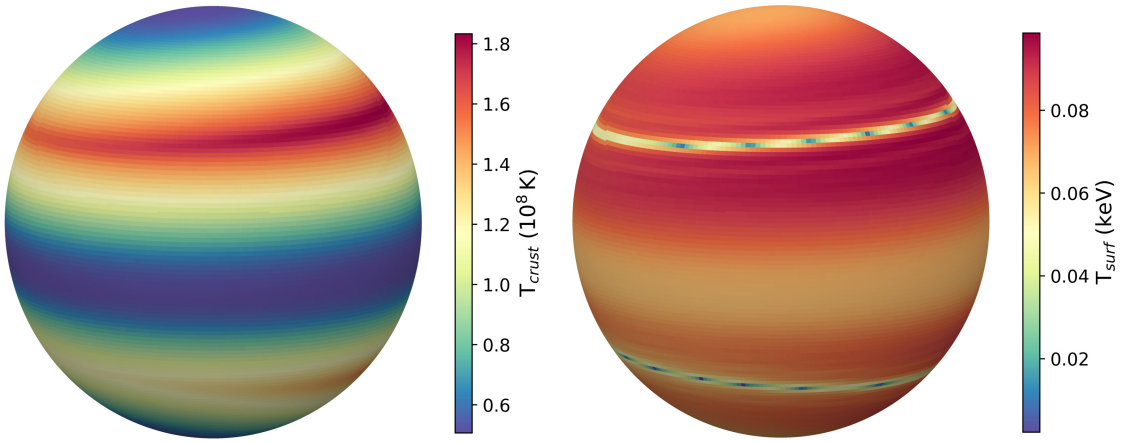

Figure 5.11: Temperature maps at the top of the crust (left) and on the NS surface (right) after $t \simeq 10^4$ yr for the same run as in Figure 5.9 (run45B10).

These structures reflect into an hotter belt at colatitude $\approx \pi - \Theta_B$ in the temperature map of the crust (Figure 5.8) since the heat tends to be transported along the field lines (2.23). Unlike the case of a purely dipolar field (5.1.1), the presence of the misaligned quadrupole makes the belt non-uniform and asymmetric. The net effect is the creation of a spot in the northern hemisphere which is hotter than the belt and the other regions of the NS crust and its evolution is shown in Figure 5.7. The thickness of the hot belt tends to decrease as the NS cools down, and the temperature tends to become more and more uniform.

Figure 5.8 shows the temperature map of the crust (right panel) and the temperature distribution on the NS surface considering the effects of the envelope (left panel). The surface temperature map is inverted with respect to the crust one, i.e. the crust temperature is smaller in regions where the magnetic field is nearly radial, while it is larger in the regions with an almost tangential field. The heat flux is suppressed most severely in the envelope and causes the decrease of the temperature gradient in the equatorial regions where the field is tangential, so that a variation of the crust temperature on the magnetic poles, where the field lines are radial, is

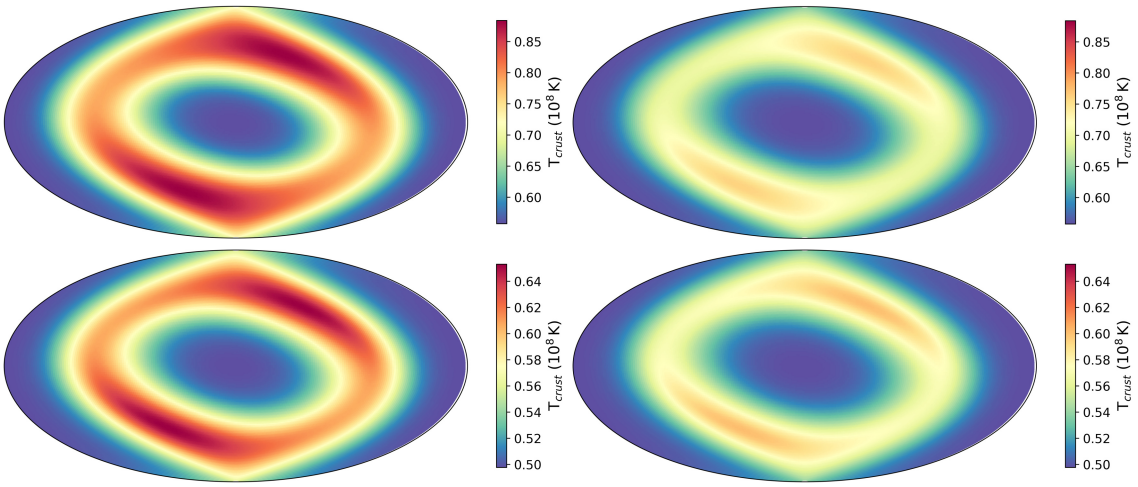

Figure 5.12: Evolution of the temperature (Mollweide projection) at the top of the crust for run90B1, see Table 5.1. Time increases from left to right and from top to bottom. Snapshots are separated by $\approx$ 4000 yr and the first one (top left) is at $t \approx 5000$ yr. Note that the colour bar range decreases between the top and the bottom row to improve visualisation.

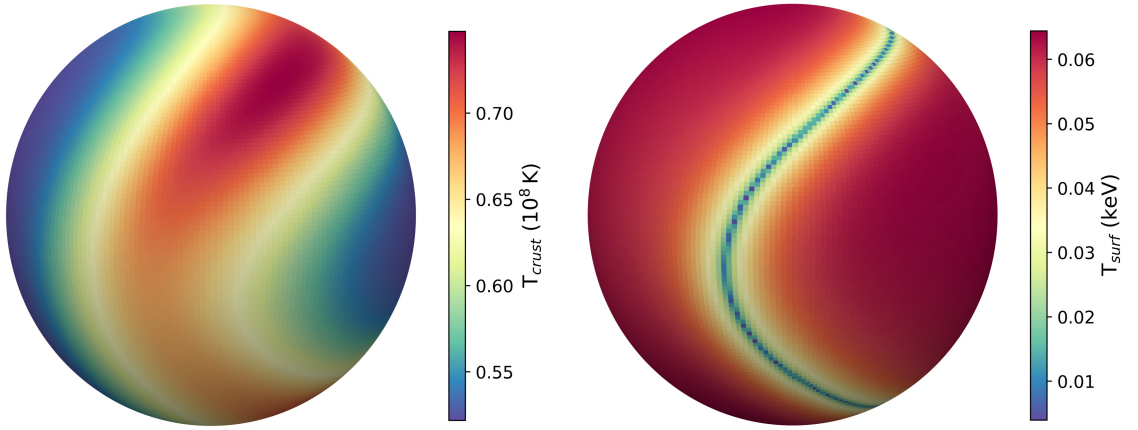

Figure 5.13: Temperature maps at the top of the crust (left) and on the NS surface (right) after $t \simeq 10^4$ yr for the same run as in Figure 5.12 (run90B1).

higher than the equatorial one (Kondratyev et al., 2020). The surface temperature distribution, hence, is characterized by a small cold belt, which becomes irregular in shape with respect to the case of a pure-dipolar configuration tilted by Θ_B if the parameter $\beta_B \lesssim 1$.

By increasing the value of the quadrupole field, i.e. by increasing the value of β_B, a second hotter belt appears in the temperature distribution of the crust and its shape is more circular. We consider, indeed, a configuration with a quadrupole much stronger than the dipolar component, hence $\beta_B = 10$ (run45B10), and $\Theta_B = 45°$ to have a direct comparison with the previous example (run45B0.75).

As in the previous cases, the radial component decreases in time since its energy is transferred to the θ and ϕ components. Moreover, due to the Hall term (3.12), some belts in which the magnetic field is stronger arise at latitude $\approx \Theta_B$ both in the northern and southern hemisphere. The general magnetic topology is quite different from the one of the previous run (run45B0.75) and it tends to approach the pure-quadrupolar case, which is characterized by a crustal temperature map with two parallel hotter belt, one in each hemisphere.

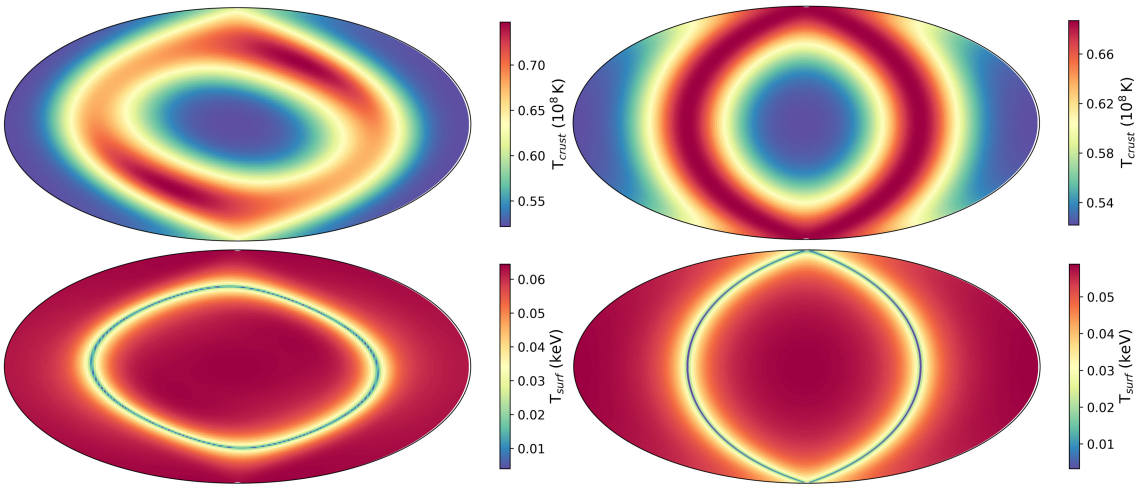

Figure 5.14: Comparison between plots of the temperature (Mollweide projection) at the top of the crust (top row) and on the NS surface (bottom row) for the same run as in Figure 5.12 (left) and the same configuration without the quadrupole component (right).

The effect of the dipole field is clearly evident when looking at the crustal and surface temperature maps after $\approx 10^4$ yr (Figure 5.11): the two hotter belts are not uniform and the one in the northern hemisphere is hotter and thicker than the other due to the presence of the dipolar component. Considering the effects of the envelope, the surface temperature map is inverted with respect to the crustal one, i.e. two small colder belt arise at colatitude $\approx \pi - \Theta_B$. The belt in the northern hemisphere is surrounded by hotter regions reaching values of ≈ 0.08 keV while the same structures in the southern region are colder.

The evolution in time of the belt structures is shown in Figure 5.10, where the initial snapshot corresponds to the configuration after ≈ 2000 yr and the other plots are separated by ≈ 8000 yr. The shape of the hotter belts becomes more and more narrow, non-uniform and non-circular while the hotter spot remains in the northern region.

As final case is the one with a dipole field rotated by $\Theta_B = 90°$ with respect to a quadrupole and relative strenght $\beta_B = 1$ (run90B1). This configuration is interesting to see the effect of quadrupole perpendicular to a dipolar field for which we expect an equatorial hotter belt in the crust (Figure 5.2). Since the dipole is tilted by 90°, the hotter belt should be not on the equatorial region but along the meridians at $\phi = \pm 90°$. The effect of the quadrupole changes the crustal temperature distribution so that the belt shape is more like a "jaw" and not along the meridian, as shown in Figure 5.13.

Moreover, the belt is not uniform in temperature but two hotter spots can be identified one in each hemisphere, unlike the case of a pure dipole with axis tilted by 90° (Figure 5.14, right panels). The hot belt evolution in time is shown in Figure 5.12. As in the previous cases, run45B0.75 and run45B10, the thickness of the hotter belt tends to decrease in time as it cools down maintaining its general shape. The hotter region in crustal temperature map reflects into a small colder belt on the surface as in the previous case due to the effects of the NS envelope (Figure 5.13).

An intriguing question is whether configurations characterized by a tilted component are stable or if the multipoles tend to align. We can extract from the code the angles between the dipole and the quadrupole, respectively $\Theta_{\rm Dip}$ and $\Theta_{\rm Quad}$, with respect to the z-axis at each timestep. Hence, the parameter $\Theta_B = \Theta_{\rm Dip} - \Theta_{\rm Quad}$ can be followed in time. In particular, we consider three different runs (Table 5.1)

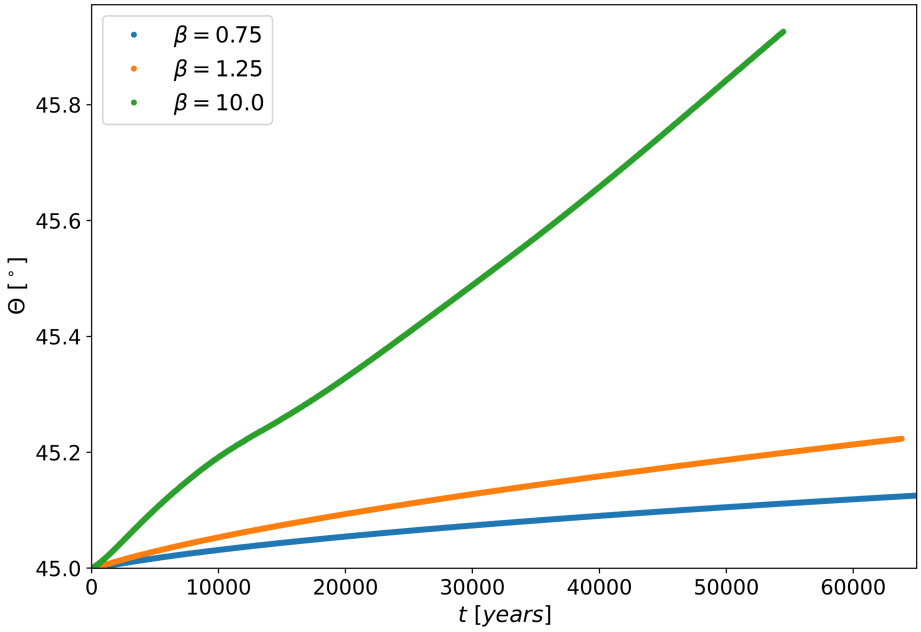

Figure 5.15: Evolution in time of the parameter Θ_B for three different magnetic field initial configurations.

starting from configurations with the same initial $\Theta_B = 45°$ but different values of β_B (Figure 5.15).

The disalignment Θ_B tends to grow in time and its increase depends on the value of tha parameter β_B. However, the change in Θ_B is quite modest ($\lesssim 2$ %) over all the timespan of our simulations. The bigger β_B, the bigger the change, but even in the case of run45B10 with $\beta_B = 10$, the increase does not exceed $\approx 1°$ in about 5×10^4 yr years of evolution.

We checked the behaviour in time of the disalignment Θ_B also for run90B1 and, as in the previous cases, we found that the dipole remain perpendicular to the quadrupole for all the simulated time (5×10^4 yr) up to machine precision.

Hence, the dipolar component does not tend to realign with the quadrupole in an astrophysically relevant timescale and the magnetic field configuration can be considered quite stable with respect to the magnetic induction equation. However, the effect of the NS spin would make the dipole to realign with the rotation axis. Indeed, the electromagnetic radiation emitted by an oblique rotating dipole results in a torque on the star that causes the angular velocity axis to migrate through the neutron star toward alignment with the magnetic axis.

6. Conclusions and Future Perspectives

In this work, we studied the magneto-thermal evolution of isolated highly-magnetised neutron stars. After introducing the theoretical details of the Hall induction and thermal evolution equations (Chapter 3), we presented some of the first fully coupled magneto-thermal numerical simulations in three dimensions. A fully 3D, pseudo-spectral code opens up countless possibilities in the study of neutron star magneto-thermal evolution.

Owing to the inherent numerical complexity, the present version of the PARODY code has nevertheless some limitations. In fact, we had to reduce the microphysical input to a realistic yet unsophisticated model for the computing time to be manageable. This concerns in particular the use of a simplified form for the hydrostatic equilibrium density profile of equation (3.22), which was also assumed independent on temperature and magnetic field, that has not been obtained from a realistic equation of state of ultradense matter, and the use of a constant τ throughout the crust. Other strong prescriptions come from the boundary conditions (4.8). As already mentioned in section 4.3, the condition on the magnetic fields at the crust-core interface assumes that the core is a Type I superconductor, so that no magnetic field is allowed to penetrate it. However, the question of which is the superconducting phase of the NS core is still a hotly debated one. Would the core be a Type II supeconductor then some field lines can enter in the core (see e.g. Baym et al., 1969).

6.1 Discussion

As a benchmark, we started from an axisymmetric configuration of the magnetic field, checking the existence of a stable solution after a few τ_H, the Hall attractor, for which the magnetic field is dominated by odd modes. A NS will spend about a Myr of its life in the attractor stage, until the Ohmic dissipation starts to dominate. The magnetic field is stronger near the equator, where the field lines close up. Hence, heat is trapped in the equatorial region since it tends to follow the magnetic field lines (Figure 5.2). The surface temperature map for this configuration (Figure 5.5) is quite similar, as expected, to the one obtained for a purely-dipolar field (Figure 5.2) and it exhibits a small colder belt along the equator, surrounded by two hotter regions.

Then, we presented some of the first 3D numerical simulations of the coupled magneto-thermal evolution starting from a non-axisymmetric configuration for the magnetic field. The temperature maps at the top of the crust and on the NS surface are derived for magnetic topologies characterized by a dipole and a quadrupole with axes tilted by an angle Θ_B and different relative strenghts β_B. The temperature distribution reflects the magnetic field configuration, so that its general structure is determined by the dominant component between the dipole and the quadrupole

while the other makes the hotter region non-uniform and irregular in shape.

Unlike the axisymmetric configurations, in which a hot equatorial belt is persistent in time, we show that in non-axisymmetric cases the hotter structures survive only for few τ_H, and the crust becomes almost isothermal afterwards (see Figures 5.7, 5.10, 5.12).

The reason is two-fold: first, a more complex magnetic field does not allow the flow of strong, large scale currents throughout the crust (as the one flowing around the equator in the dipolar case) that can efficiently heat the crust. Second, when the structure of the field lines is more complex there are less closed lines, which act as a thermal insulator for the region they enclose. Hence, we expect that in general a highly multipolar and asymmetric field configuration translates in a more complex thermal structure of the crust in the early stages ($t \lesssim \tau_H$), but in a nearly isothermal crust in the later times.

6.2 Future Applications

Cooling, isolated NSs have the right temperature, a few MK, to shine at X-ray energies (0.1 - 10 keV) for millions of years. Surface temperature maps are a key ingredient in modelling the emission of objects, such as X-ray pulsars and the XDINS (X-ray dim isolated neutron stars). The XDINSs, known also as *The Magnificent Seven* (M7) (Treves et al., 2001), are isolated, middle aged NS exhibiting a very soft, purely thermal X-ray spectrum with typical temperatures in the range of $\sim 0.05 - 0.1$ keV and a very large X-ray-to-optical flux ratio.

The spin-down measure of the dipole field in the M7 gives values somewhat in excess of those typical of radio pulsars and not too far from those of magnetars ($\approx 10^{13}$ G), but none of them exhibits magnetar-like activity (Turolla, 2009). This led to the suggestion that the M7 could be elderly magnetars, kept hotter than normal isolated NSs of comparable age by field decay (see e.g. Pons et al., 2007). Different sources among the M7 can be at different evolutionary stages, and so they can be closer or farther from the Hall attractor stage.

Although the emerging spectrum is thermal, it is not a blackbody because their (thermal) emission can originate either in an atmosphere covering the star surface, or in a condensate (see e.g. Turolla, 2009). At any rate, the observed spectrum will produced by the superposition of the emission from those patches which are in view, each with a different value of the temperature and magnetic field.

The observed flux can be calculated at each spin phase γ, if the specific intensity I_ν is known

$$F_\nu(\gamma) = (1-x)\frac{R_{\rm NS}^2}{D^2}\int_0^{2\pi} d\Phi \int_0^1 I_\nu(\boldsymbol{k},\theta,\phi)\, du^2 \ , \tag{6.1}$$

where $R_{\rm NS}$, $M_{\rm NS}$ are the NS mass and radius, $x = R_s/R_{\rm NS}$ with $R_s = 2GM_{\rm NS}/c^2$ and D is the source distance (Zane and Turolla, 2006). The previous expression accounts also for general-relativistic effects (ray-bending) produced by the star strong gravity. The specific intensity I_ν depends, in general, on the photon direction $\boldsymbol{k}$ and on position of the emitting point on the surface, i.e. on θ and ϕ. However, the components of $\boldsymbol{k}$, θ and ϕ can be expressed in terms of γ, the colatitude and the azimuthal angle relative to the line of sight (LOS) Θ and Φ, and two geometrical angles χ and ξ which give, respectively, the inclination of the LOS and of the magnetic axis with respect to the star spin axis. We plan to extend this formalism to compute synthetic spectra and light curves starting from our 3D surface temperature maps

for non-axisymmetric configurations.

Pulse profiles produced by the thermal surface distribution induced by a simple core-centred dipolar magnetic field were investigated by Page (1995), under the assumption that each surface patch emits (isotropic) blackbody radiation. The pulse shape is always symmetrical, regardless of the viewing geometry if the temperature distribution is itself symmetric.

However it seems difficult to explain the quite large pulsed fraction and the pulse asymmetry observed in XDINSs by assuming that the thermal surface distribution is induced by a simple dipolar magnetic field. In this respect, the non-axysimmetric models we considered are indedd promising, since it has been shown that the presence of multipolar componentes induces large temperature variations even between nearby regions (Zane and Turolla, 2006).

Recently, Kondratyev et al. (2020) calculated thermal light curves using a composite black-body model starting from computed surface temperature distribution, similar to those presented in section 5.2, but not taking into account GR effects. In particular, the misaligned quadrupole influences the light curves by enhancing the pulsed fraction and changing also the shape of the pulse profiles, as well as making it non-symmetric. Hence, the existence of a quadrupolar component in the magnetic field can be also detectable, because the light curves differ both from the pure-dipolar ones and ones with inclusion of the coaxial toroidal in the NS crust.

The next step is to built thermal light curves and compare them with real observations, considering e.g. RX J1856.5-3754 since its spectral properties are very well characterized. RX J1856.5-3754 is the prototype and the brightest member of M7 and may be representatives of sources close to the Hall equilibrium. In particular, the goal is to check if RX J1856.5-3754 properties are indeed compatible with the crustal distribution of temperature and magnetic field predicted by our non-axisymmetric simulations.

Appendix

Some useful definitions and properties of special functions are illustrated in this Appendix. Legendre polynomials are used to define the spherical harmonics Y_l^m (Section 4.1) which constitutes the basis of our decomposition. Then, spherical Bessel functions are introduced in order to derive the general form of the harmonic decomposition of the initial poloidal and toroidal component as solution of the Grad-Shafranov equation (Section 4.4).

A.1 Legendre Polynomials

The Legendre polynomials $P_l(\mu)$ are a system of complete and orthogonal polynomials which satisfy the *Legendre's differential equation* in the domain $\mu \in [-1, 1]$ (Olver et al., 2010)

$$\frac{d}{d\mu}\left[(1-\mu^2)\frac{dP_l(\mu)}{d\mu}\right] + l(l+1)P_l(\mu) = 0 \ . \tag{A.1}$$

Each Legendre polynomial $P_l(\mu)$ is an l^{th}-degree polynomial and can be expressed using Rodrigues' formula

$$P_l(\mu) = \frac{1}{2^l\, l!}\frac{d^l}{d\mu^l}\left[(\mu^2-1)^l\right] \ . \tag{A.2}$$

Since they are orthogonal, the following relation holds:

$$\int_{-1}^{1} P_l(\mu)P_{l'}(\mu)d\mu = \frac{2}{2l+1}\delta_{ll'} \ , \tag{A.3}$$

where $\delta_{ll'}$ is the Kronecker delta. The associated Legendre polynomials P_l^m of degree l and order m is defined as

$$P_l^m(x) = (-1)^m(1-x^2)^{m/2}\frac{d^m}{dx^m}P_l(x) \tag{A.4}$$

and can be used to define the spherical harmonics. The associated Legendre polynomials are the canonical solutions of the *general Legendre equation*

$$\frac{d}{d\mu}\left[(1-\mu^2)\frac{d}{d\mu}P_l^m(\mu)\right] + \left[l(l+1) - \frac{m^2}{1-\mu^2}\right]P_l^m(\mu) = 0 \ . \tag{A.5}$$

When m is zero and l an integer, these functions corresponds to the Legendre polynomials. For the associated Legendre polynomials, assuming $0 \leq m \leq l$, the orthogonality conditions for fixed m reads

$$\int_{-1}^{1} P_l^m(\mu)P_{l'}^m(\mu)d\mu = \frac{2(l+m)!}{(2l+1)(l-m)!}\delta_{ll'} \ . \tag{A.6}$$

The behaviour of the associated Legendre polynomials as function of μ is shown in Figure A.1 for the first five degrees l given $m = 0, 1, 2$.

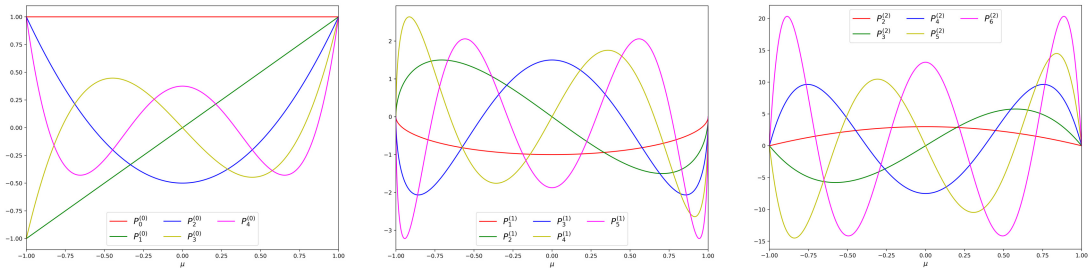

Figure A.1: Plots of the associated Legendre polynomials for $m = 0$ (left), $m = 1$ (center) and $m = 2$ (right) as function of $\mu \in [-1, 1]$.

A.2 Spherical Bessel Functions

The Bessel equation arises when finding separable solutions to the Laplace equation and the Helmholtz equation in cylindrical or spherical coordinates. Bessel functions are canonical solutions $y(x)$ of *Bessel differential equation* (Olver et al., 2010)

$$x^2 \frac{d^2y}{dx^2} + x\frac{dy}{dx} + (x^2 - \alpha^2)y = 0 \tag{A.7}$$

for an arbitrary complex number α, which defines the order of the Bessel function. Because this is a second-order linear differential equation, there must be two linearly independent solutions.

The general solution of the Bessel equation can be found as a linear combination of Bessel functions of the first J_α and second Y_α kind

$$y(x) = \mathcal{A}J_\alpha(x) + \mathcal{B}Y_\alpha(x) \tag{A.8}$$

where $\mathcal{A}$ and $\mathcal{B}$ are arbitrary constants. The Bessel functions of the first kind $J_\alpha(x)$ are non-singular at the origin ($x = 0$) for integer or positive α and are defined by the infinite power series expansion

$$J_\alpha(x) = \sum_{k=0}^{\infty} \frac{(-1)^m}{m!\,\Gamma(k+\alpha+1)} \left(\frac{x}{2}\right)^{2m+\alpha} = \sum_{k=0}^{\infty} \frac{(-1)^m}{m!(k+\alpha)!} \left(\frac{x}{2}\right)^{2m+\alpha} \tag{A.9}$$

where $\Gamma(z)$ is the gamma function. The Bessel functions of the second kind Y_α, also known as Weber or Neumann functions, are singular at $x = 0$ and are related to the Bessel function of the first kind as follows

$$Y_\alpha(x) = \frac{J_\alpha(x)\cos(\alpha\pi) - J_{-\alpha}(x)}{\sin(\alpha\pi)} \ . \tag{A.10}$$

Solving the Helmholtz equation in spherical coordinates, the radial equation has the form

$$x^2 \frac{d^2y}{dx^2} + x\frac{dy}{dx} + [x^2 - n(n+1)]y = 0 \tag{A.11}$$

and two linearly independent solutions to this equation are the so-called *spherical Bessel functions* j_l and y_l and are related to the ordinary Bessel function J_l and Y_l by

$$\begin{aligned} j_l(x) &= \sqrt{\frac{\pi}{2x}} J_{l+\frac{1}{2}}(x) \ , \\ y_l(x) &= \sqrt{\frac{\pi}{2x}} Y_{l+\frac{1}{2}}(x) = (-1)^{l+1}\sqrt{\frac{\pi}{2x}} J_{-l-\frac{1}{2}}(x) \ . \end{aligned} \tag{A.12}$$

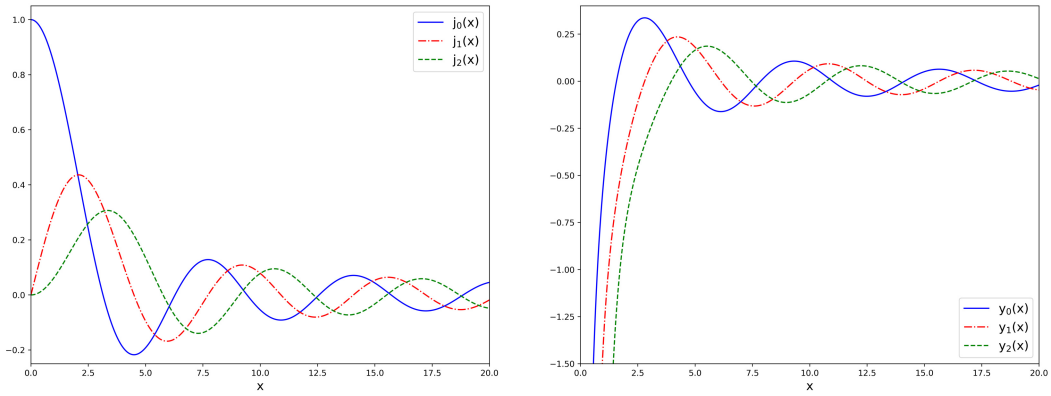

Figure A.2: Plots of spherical Bessel function j_l (right panel) and y_l (left panel) of order $l = 0, 1, 2$.

The spherical Bessel functions can be also recast as (*Rayleigh's formulas*)

$$\begin{aligned} j_l(x) &= (-x)^l \left(\frac{1}{x}\frac{d}{dx}\right)^l \frac{\sin x}{x} \ , \\ y_l(x) &= -(-x)^l \left(\frac{1}{x}\frac{d}{dx}\right)^l \frac{\cos x}{x} \ . \end{aligned} \tag{A.13}$$

The trend of the spherical Bessel functions j_l and y_l of order $l = 0, 1, 2$ is shown in Figure A.2 and both tend to 0 for large x. Moreover, j_l is always finite as the Bessel function of the first kind while y_l diverges for $x \to 0$.

A.3 Jacobi Polynomials

The Jacobi polynomials $P_n^{(a,b)}(z)$ are a class of orthogonal polynomials which are solutions to the Jacobi differential equation:

$$(1 - z^2)y'' + [b - a - (a + b + 2)z]y' + n(n + a + b + 1)y = 0 \ . \tag{A.14}$$

Using the Rodrigues' formula, the Jacobi polynomials can be defined as

$$P_n^{(a,b)}(z) = \frac{(-1)^n}{2^n n!}(1 - z)^{-a}(1 + z)^{-b}\frac{d^n}{dz^n}\left[(1 - z)^a(1 + z)^b(1 - z^2)^n\right] \ , \tag{A.15}$$

and, if $a = b = 0$, then these polynomials reduce to the Legendre polynomials (A.2). The Wigner (small) matrix $d_{nm}^{(l)}$ can be defined in terms of Jacobi polynomials as (Biedenharn and Louck, 1981)

$$d_{nm}^{(l)}(\beta) = \sqrt{\frac{(l + m)!(l - m)!}{(l + n)!(l - n)!}}\left(\sin\frac{\beta}{2}\right)^{m-n}\left(\cos\frac{\beta}{2}\right)^{m+n} P_{l-m}^{(m-n,m+n)}(\cos\beta) \ . \tag{A.16}$$

Bibliography

J. Aubert, J. Aurnou, and J. Wicht. "The magnetic structure of convection-driven numerical dynamos". *Geophysical Journal International*, 172(3):945–956, 2008. doi: 10.1111/j.1365-246X.2007.03693.x. URL https://onlinelibrary.wiley.com/doi/abs/10.1111/j.1365-246X.2007.03693.x.

W. Baade and F. Zwicky. "Remarks on Super-Novae and Cosmic Rays". *Physical Review*, 46(1):76–77, 1934. doi: 10.1103/PhysRev.46.76.2.

J. Bardeen, L. N. Cooper, and J. R. Schrieffer. "Theory of Superconductivity". *Phys. Rev.*, 108:1175–1204, 1957. doi: 10.1103/PhysRev.108.1175. URL https://link.aps.org/doi/10.1103/PhysRev.108.1175.

G. Baym, C. Pethick, D. Pines, and M. Ruderman. "Spin Up in Neutron Stars : The Future of the Vela Pulsar". *Nature*, 224(5222):872–874, Nov 1969. ISSN 1476-4687. doi: 10.1038/224872a0. URL https://doi.org/10.1038/224872a0.

G. Baym, C. Pethick, and P. Sutherland. "The Ground State of Matter at High Densities: Equation of State and Stellar Models". *Astrophys. J.*, 170:299, 1971. doi: 10.1086/151216.

H. A. Bethe and C. L. Critchfield. "The Formation of Deuterons by Proton Combination". *Phys. Rev.*, 54:248–254, Aug 1938. doi: 10.1103/PhysRev.54.248. URL https://link.aps.org/doi/10.1103/PhysRev.54.248.

L. Biedenharn and J. D. Louck. *"Angular momentum in quantum physics"*. AW, 1981. ISBN 9780201135077,0201135078.

A. Bohr, B. R. Mottelson, and D. Pines. "Possible Analogy between the Excitation Spectra of Nuclei and Those of the Superconducting Metallic State". *Phys. Rev.*, 110:936–938, 1958. doi: 10.1103/PhysRev.110.936. URL https://link.aps.org/doi/10.1103/PhysRev.110.936.

E. Braaten and D. Segel. "Neutrino energy loss from the plasma process at all temperatures and densities". *Physical Review D*, 48(4):1478–1491, 1993. ISSN 0556-2821. doi: 10.1103/physrevd.48.1478. URL http://dx.doi.org/10.1103/PhysRevD.48.1478.

B. Carter and D. Langlois. "Relativistic models for superconducting-superfluid mixtures". *Nuclear Physics B*, 531(1-3):478–504, 1998. ISSN 0550-3213. doi: 10.1016/s0550-3213(98)00430-1. URL http://dx.doi.org/10.1016/S0550-3213(98)00430-1.

N. Chamel and P. Haensel. "Physics of Neutron Star Crusts". *Living Reviews in Relativity*, 11(1), 2008. ISSN 1433-8351. doi: 10.12942/lrr-2008-10. URL http://dx.doi.org/10.12942/lrr-2008-10.

S. Chandrasekhar and P. C. Kendall. "On Force-Free Magnetic Fields.". *Astrophys. J.*, 126:457, 1957. doi: 10.1086/146413.

H.-Y. Chiu and P. Morrison. "Neutrino Emission from Black-Body Radiation at High Stellar Temperatures". *Phys. Rev. Lett.*, 5:573–575, 1960. doi: 10.1103/PhysRevLett.5.573.

L. N. Cooper. "Bound Electron Pairs in a Degenerate Fermi Gas". *Phys. Rev.*, 104: 1189–1190, 1956. doi: 10.1103/PhysRev.104.1189. URL `https://link.aps.org/doi/10.1103/PhysRev.104.1189`.

D. De Grandis, R. Turolla, T. S. Wood, S. Zane, R. Taverna, and K. N. Gourgouliatos. "3D modelling of magneto-thermal evolution of neutron stars: method and test cases". *Astrophys. J., in press*, 2020.

E. Dormy, P. Cardin, and J. Jault. "MHD flow in a slightly differentially rotating spherical shell, with conducting inner core, in a dipolar magnetic field". *Earth and Planetary Science Letters*, 160(1):15 – 30, 1998. ISSN 0012-821X. doi: https://doi.org/10.1016/S0012-821X(98)00078-8. URL `http://www.sciencedirect.com/science/article/pii/S0012821X98000788`.

F. Douchin and P. Haensel. "Inner edge of neutron-star crust with SLy effective nucleon-nucleon interactions". *Physics Letters B*, 485(1-3):107–114, 2000. URL `http://dx.doi.org/10.1016/S0370-2693(00)00672-9`.

J. R. Driscoll and D. M. Healy. "Computing Fourier Transforms and Convolutions on the 2-Sphere". *Advances in Applied Mathematics*, 15(2):202 – 250, 1994. ISSN 0196-8858. doi: https://doi.org/10.1006/aama.1994.1008. URL `http://www.sciencedirect.com/science/article/pii/S0196885884710086`.

R. C. Duncan and C. Thompson. "Formation of Very Strongly Magnetized Neutron Stars: Implications for Gamma-Ray Bursts". *Astrophys. J.*, 392:L9, 1992. doi: 10.1086/186413.

B. L. Friman and O. V. Maxwell. "Neutrino emissivities of neutron stars.". *Astrophys. J.*, 232:541–557, 1979. doi: 10.1086/157313.

U. Geppert and H. J. Wiebicke. "Amplification of neutron star magnetic fields by thermoelectric effects. I - General formalism". *Astron. & Astrophys. Suppl. Ser.*, 87(2):217–228, 1991.

P. Goldreich and W. H. Julian. "Pulsar Electrodynamics". *Astrophys. J.*, 157:869, 1969. doi: 10.1086/150119.

P. Goldreich and A. Reisenegger. "Magnetic Field Decay in Isolated Neutron Stars". *Astrophys. J.*, 395:250, 1992. doi: 10.1086/171646.

K. N. Gourgouliatos and A. Cumming. "Hall effect in neutron star crusts: evolution, endpoint and dependence on initial conditions". *Monthly Notices of the Royal Astronomical Society*, 438(2):1618–1629, 12 2013. doi: 10.1093/mnras/stt2300. URL `https://doi.org/10.1093/mnras/stt2300`.

K. N. Gourgouliatos and A. Cumming. "Hall Attractor in Axially Symmetric Magnetic Fields in Neutron Star Crusts". *Physical Review Letters*, 112(17), 2014. ISSN 1079-7114. doi: 10.1103/physrevlett.112.171101. URL `http://dx.doi.org/10.1103/PhysRevLett.112.171101`.

K. N. Gourgouliatos, T. S. Wood, and R. Hollerbach. "Magnetic field evolution in magnetar crusts through three-dimensional simulations". *Proceedings of the National Academy of Sciences*, 113(15):3944–3949, 2016. ISSN 1091-6490. doi: 10.1073/pnas.1522363113. URL http://dx.doi.org/10.1073/pnas.1522363113.

E. H. Gudmundsson, C. J. Pethick, and R. I. Epstein. "Structure of neutron star envelopes". *Astrophys. J.*, 272:286–300, 1983. doi: 10.1086/161292.

P. Haensel, A. D. Kaminker, and D. G. Yakovlev. "Electron neutrino-antineutrino bremsstrahlung in a liquid phase of neutron star crusts.". *Astron. & Astrophys.*, 314:328–340, 1996.

P. Haensel, A. Y. Potekhin, and D. G. Yakovlev. "Neutron stars 1: Equation of state and structure". *Astrophys. Space Sci. Libr.*, 326, 2007. doi: 10.1007/978-0-387-47301-7.

B. Haskell, D. I. Jones, and N. Andersson. "Mountains on neutron stars: accreted versus non-accreted crusts". *Monthly Notices of the Royal Astronomical Society*, 373(4):1423–1439, 2006. ISSN 1365-2966. doi: 10.1111/j.1365-2966.2006.10998.x. URL http://dx.doi.org/10.1111/j.1365-2966.2006.10998.x.

A. Hewish, S. J. Bell, J. D. H. Pilkington, P. F. Scott, and R. A. Collins. "Observation of a Rapidly Pulsating Radio Source". *Nature*, 217(5130):709–713, 1968. doi: 10.1038/217709a0.

W. C. G. Ho, K. Glampedakis, and N. Andersson. "Magnetars: super(ficially) hot and super(fluid) cool". *Monthly Notices of the Royal Astronomical Society*, 422(3): 2632–2641, 2012. ISSN 0035-8711. doi: 10.1111/j.1365-2966.2012.20826.x. URL https://doi.org/10.1111/j.1365-2966.2012.20826.x.

R. Hollerbach and G. Rüdiger. "The influence of Hall drift on the magnetic fields of neutron stars". *Monthly Notices of the Royal Astronomical Society*, 337(1): 216–224, 11 2002. ISSN 0035-8711. doi: 10.1046/j.1365-8711.2002.05905.x. URL https://doi.org/10.1046/j.1365-8711.2002.05905.x.

R. Hollerbach and G. Rüdiger. "Hall drift in the stratified crusts of neutron stars". *Monthly Notices of the Royal Astronomical Society*, 347(4):1273–1278, 02 2004. ISSN 0035-8711. doi: 10.1111/j.1365-2966.2004.07307.x. URL https://doi.org/10.1111/j.1365-2966.2004.07307.x.

A. D. Kaminker, K. P. Levenfish, and D. G. Yakovlev. "Synchrotron Emission of Neutrino Pairs in Neutron Stars". *Soviet Astronomy Letters*, 17:450, 1991.

A. D. Kaminker, O. Y. Gnedin, D. G. Yakovlev, P. Amsterdamski, and P. Haensel. "Neutrino emissivity from e^-e^+ annihilation in a strong magnetic field: Hot, non-degenerate plasma". *Phys. Rev. D*, 46:4133–4139, 1992. doi: 10.1103/PhysRevD.46.4133. URL https://link.aps.org/doi/10.1103/PhysRevD.46.4133.

A. D. Kaminker, C. J. Pethick, A. Y. Potekhin, V. Thorsson, and D. G. Yakovlev. "Neutrino-pair bremsstrahlung by electrons in neutron star crusts". *Astron. & Astrophys.*, 343:1009–1024, 1999.

Kaminker, A. D., Haensel, P., and Yakovlev, D. G. "Nucleon superfluidity vs. observations of cooling neutron stars". *Astron. & Astrophys.*, 373(2):L17–L20, 2001. doi: 10.1051/0004-6361:20010713. URL https://doi.org/10.1051/0004-6361:20010713.

E. M. Kantor and M. E. Gusakov. "The neutrino emission due to plasmon decay and neutrino luminosity of white dwarfs". *Monthly Notices of the Royal Astronomical Society*, 381(4):1702–1710, 2007. ISSN 0035-8711. doi: 10.1111/j.1365-2966.2007.12342.x. URL https://doi.org/10.1111/j.1365-2966.2007.12342.x.

I. A. Kondratyev, S. G. Moiseenko, G. S. Bisnovatyi-Kogan, and M. V. Glushikhina. "Three-dimensional heat transfer effects in external layers of a magnetized neutron star". *Monthly Notices of the Royal Astronomical Society*, 497(3):2883–2892, Jul 2020. ISSN 1365-2966. doi: 10.1093/mnras/staa2154. URL http://dx.doi.org/10.1093/mnras/staa2154.

L. Landau. "On the theory of stars". *Phys. Z. Sowjetunion*, 1:285–288, 1932.

J. M. Lattimer, C. J. Pethick, M. Prakash, and P. Haensel. "Direct URCA process in neutron stars". *Phys. Rev. Lett.*, 66:2701–2704, 1991. doi: 10.1103/PhysRevLett.66.2701. URL https://link.aps.org/doi/10.1103/PhysRevLett.66.2701.

K. P. Levenfish and D. G. Yakovlev. "Specific heat of neutron star cores with superfluid nucleons". *Astronomy Reports*, 38(2):247–251, 1994.

B. C. Low and Y. Q. Lou. "Modeling Solar Force-free Magnetic Fields". *Astrophys. J.*, 352:343, 1990. doi: 10.1086/168541.

A. B. Migdal. "Superfluidity and the Moments of Inertia of Nuclei". *Soviet Physics JETP*, 37 (10):249–263, 1960.

C. W. Misner, K. Thorne, and J. Wheeler. *"Gravitation"*. W. H. Freeman, San Francisco, 1973. ISBN 978-0-7167-0344-0, 978-0-691-17779-3.

J. W. Negele and D. Vautherin. "Neutron star matter at sub-nuclear densities". *Nucl. Phys.*, 207(2), 1973. doi: 10.1016/0375-9474(73)90349-7.

W. G. Newton, M. Gearheart, J. Hooker, and B.-A. Li. "The nuclear symmetry energy, the inner crust, and global neutron star modeling". *Nova Science*, 2011.

D. D. Ofengeim, A. D. Kaminker, and D. G. Yakovlev. "Neutrino-pair bremsstrahlung in a neutron star crust". *EPL (Europhysics Letters)*, 108(3): 31002, 2014. ISSN 1286-4854. doi: 10.1209/0295-5075/108/31002. URL http://dx.doi.org/10.1209/0295-5075/108/31002.

F. W. Olver, D. W. Lozier, R. F. Boisvert, and C. W. Clark. *"NIST Handbook of Mathematical Functions"*. Cambridge University Press, USA, 1st edition, 2010. ISBN 0521140633.

J. R. Oppenheimer and G. M. Volkoff. "On Massive Neutron Cores". *Physical Review*, 55(4):374–381, 1939. doi: 10.1103/PhysRev.55.374.

D. Page. Surface Temperature of a Magnetized Neutron Star and Interpretation of the ROSAT Data. I. Dipolar Fields. *Astrophys. J.*, 442:273, 1995. doi: 10.1086/175439.

D. Page. *"Neutron Star Cooling: I"*, pages 247–288. Springer Berlin Heidelberg, Berlin, Heidelberg, 2009. ISBN 978-3-540-76965-1. doi: 10.1007/978-3-540-76965-1_11. URL https://doi.org/10.1007/978-3-540-76965-1_11.

D. Page. "NSCool: Neutron star cooling code", 2016.

D. Page, U. Geppert, and T. Zannias. "General relativistic treatment of the thermal, magnetic and rotational evolution of isolated neutron stars with crustal magnetic fields". *Astron. & Astrophys.*, 360:1052–1066, 2000.

D. Page, J. M. Lattimer, M. Prakash, and A. W. Steiner. "Minimal Cooling of Neutron Stars: A New Paradigm". *The Astrophysical Journal Supplement Series*, 155(2):623–650, 2004. ISSN 1538-4365. doi: 10.1086/424844. URL http://dx.doi.org/10.1086/424844.

L. Pavan, R. Turolla, S. Zane, and L. Nobili. "Topology of magnetars external field – I. Axially symmetric fields". *Monthly Notices of the Royal Astronomical Society*, 395(2):753–763, 2009. ISSN 0035-8711. doi: 10.1111/j.1365-2966.2009.14600.x. URL https://doi.org/10.1111/j.1365-2966.2009.14600.x.

J. A. Pons and U. Geppert. "Magnetic field dissipation in neutron star crusts: from magnetars to isolated neutron stars". *Astron. & Astrophys.*, 470(1):303–315, 2007. doi: 10.1051/0004-6361:20077456.

J. A. Pons and D. Viganò. "Magnetic, thermal and rotational evolution of isolated neutron stars". *Living Reviews in Computational Astrophysics*, 5(1), 2019. ISSN 2365-0524. doi: 10.1007/s41115-019-0006-7. URL http://dx.doi.org/10.1007/s41115-019-0006-7.

J. A. Pons, B. Link, J. A. Miralles, and U. Geppert. "Evidence for Heating of Neutron Stars by Magnetic-Field Decay". *Physical Review Letters*, 98(7), 2007. ISSN 1079-7114. doi: 10.1103/physrevlett.98.071101.

S. B. Popov, R. Taverna, and R. Turolla. "Probing the surface magnetic field structure in RX J1856.5-3754". *Monthly Notices of the Royal Astronomical Society*, 464(4):4390–4398, 10 2016. ISSN 0035-8711. doi: 10.1093/mnras/stw2681. URL https://doi.org/10.1093/mnras/stw2681.

A. Y. Potekhin and D. G. Yakovlev. "Thermal structure and cooling of neutron stars with magnetized envelopes". *A&A*, 374(1):213–226, 2001. doi: 10.1051/0004-6361:20010698. URL https://doi.org/10.1051/0004-6361:20010698.

A. Y. Potekhin, J. A. Pons, and D. Page. "Neutron Stars—Cooling and Transport". *Space Science Reviews*, 191(1-4):239–291, Jul 2015. ISSN 1572-9672. doi: 10.1007/s11214-015-0180-9. URL http://dx.doi.org/10.1007/s11214-015-0180-9.

S. B. Rüster, M. Hempel, and J. Schaffner-Bielich. "Outer crust of nonaccreting cold neutron stars". *Phys. Rev. C*, 73, 2006. doi: 10.1103/PhysRevC.73.035804. URL https://link.aps.org/doi/10.1103/PhysRevC.73.035804.

G. Rüdiger and R. Hollerbach. *"Neutron Star Magnetism"*, chapter 7, pages 265–279. John Wiley & Sons, Ltd, 2005. ISBN 9783527603657. doi: 10.1002/3527603654.ch7. URL https://onlinelibrary.wiley.com/doi/abs/10.1002/3527603654.ch7.

S. Shapiro and S. Teukolsky. *"Black holes, white dwarfs, and neutron stars: The physics of compact objects"*. 1983. ISBN 978-0-471-87316-7.

K. S. Thorne. "The relativistic equations of stellar structure and evolution". *Astrophys. J.*, 212:825–831, 1977. doi: 10.1086/155108.

R. C. Tolman. "Static Solutions of Einstein's Field Equations for Spheres of Fluid". *Phys. Rev.*, 55:364–373, 1939. doi: 10.1103/PhysRev.55.364.

A. Treves, S. B. Popov, M. Colpi, M. E. Prokhorov, and R. Turolla. "The magnificent seven: close-by cooling neutron stars?". *ASP Conf. Ser.*, 234:225, 2001.

S. Tsuruta. *"Neutron Star Models"*. PhD thesis, Columbia University, New York, N.Y., 1964.

S. Tsuruta and A. G. W. Cameron. "Cooling and detectability of neutron stars". *Can. J. Phys.*, 44:1863–1894, 1966. doi: 10.1139/p66-156.

R. Turolla. *"Isolated Neutron Stars: The Challenge of Simplicity"*, volume 357 of *Astrophysics and Space Science Library*, page 141. 2009. doi: 10.1007/978-3-540-76965-1_7.

V. A. Urpin and D. G. Yakovlev. "Thermogalvanomagnetic Effects in White Dwarfs and Neutron Stars". *Soviet. Ast.*, 24:425, 1980.

D. Viganò. "Magnetic fields in neutron stars", 2013.

D. Viganò and J. A. Pons. "Central compact objects and the hidden magnetic field scenario". *Monthly Notices of the Royal Astronomical Society*, 425(4):2487–2492, 2012. ISSN 0035-8711. doi: 10.1111/j.1365-2966.2012.21679.x. URL `https://doi.org/10.1111/j.1365-2966.2012.21679.x`.

D. Viganò, N. Rea, J. A. Pons, R. Perna, D. N. Aguilera, and J. A. Miralles. "Unifying the observational diversity of isolated neutron stars via magneto-thermal evolution models". *Monthly Notices of the Royal Astronomical Society*, 434(1):123–141, 07 2013. ISSN 0035-8711. doi: 10.1093/mnras/stt1008. URL `https://doi.org/10.1093/mnras/stt1008`.

T. S. Wood and R. Hollerbach. "Three Dimensional Simulation of the Magnetic Stress in a Neutron Star Crust". *Physical Review Letters*, 114(19), 2015. ISSN 1079-7114. doi: 10.1103/physrevlett.114.191101. URL `http://dx.doi.org/10.1103/PhysRevLett.114.191101`.

D. Yakovlev, A. D. Kaminker, O. Y. Gnedin, and P. Haensel. "Neutrino emission from neutron stars". *Physics Reports*, 354(1-2):1–155, 2001. ISSN 0370-1573. doi: 10.1016/s0370-1573(00)00131-9. URL `http://dx.doi.org/10.1016/S0370-1573(00)00131-9`.

D. G. Yakovlev, W. C. G. Ho, P. S. Shternin, C. O. Heinke, and A. Y. Potekhin. "Cooling rates of neutron stars and the young neutron star in the Cassiopeia A supernova remnant". *Monthly Notices of the Royal Astronomical Society*, 411(3):1977–1988, 2010. ISSN 0035-8711. doi: 10.1111/j.1365-2966.2010.17827.x. URL `http://dx.doi.org/10.1111/j.1365-2966.2010.17827.x`.

S. Zane and R. Turolla. "Unveiling the thermal and magnetic map of neutron star surfaces though their x-ray emission: method and lightcurves analysis". *Mon. Not. Roy. Astron. Soc.*, 366:727–738, 2006. doi: 10.1111/j.1365-2966.2005.09784.x.

J. M. Ziman. *"Principles of the Theory of Solids"*. Cambridge University Press, 2 edition, 1972. doi: 10.1017/CBO9781139644075.